Finite ion temperature effects on scrape-off layer turbulence

Annamaria Mosetto, Federico D. Halpern, Sébastien Jolliet, Joaquim Loizu, and Paolo Ricci

Citation: Physics of Plasmas (1994-present) **22**, 012308 (2015); doi: 10.1063/1.4904300
View online: http://dx.doi.org/10.1063/1.4904300
View Table of Contents: http://scitation.aip.org/content/aip/journal/pop/22/1?ver=pdfcov
Published by the AIP Publishing

PHYSICS OF PLASMAS 22, 012308 (2015)

Finite ion temperature effects on scrape-off layer turbulence

Annamaria Mosetto,[a)] Federico D. Halpern, Sébastien Jolliet, Joaquim Loizu,[b)] and Paolo Ricci
École Polytechnique Fédérale de Lausanne (EPFL), Centre de Recherches en Physique des Plasmas (CRPP), CH-1015 Lausanne, Switzerland

(Received 8 August 2014; accepted 6 November 2014; published online 15 January 2015)

Ion temperature has been measured to be of the same order, or higher, than the electron temperature in the scrape-off layer (SOL) of tokamak machines, questioning its importance in determining the SOL turbulent dynamics. Here, we present a detailed analysis of finite ion temperature effects on the linear SOL instabilities, such as the resistive and inertial branches of drift waves and ballooning modes, and a discussion of the properties of the ion temperature gradient (ITG) instability in the SOL, identifying the $\eta_i = L_n/L_{T_i}$ threshold necessary to drive the mode unstable. The non-linear analysis of the SOL turbulent regimes by means of the gradient removal theory is performed, revealing that the ITG plays a negligible role in limited SOL discharges, since the ion temperature gradient is generally below the threshold for driving the mode unstable. It follows that the resistive ballooning mode is the prevailing turbulence regime for typical limited SOL parameters. The theoretical estimates are confirmed by non-linear flux-driven simulations of SOL plasma dynamics. [http://dx.doi.org/10.1063/1.4904300]

I. INTRODUCTION

In the last years, an increased effort has been devoted to the measurement of ion temperature in the tokamak scrape-off layer (SOL). While most of the experimental campaigns are based on the use of retarding field analyzer probes (see Ref. 1 and references therein for a review of measurements before 2010, and Refs. 2–6 for more recent experimental campaigns), also other techniques are employed, such as the charge-exchange recombination spectroscopy,[7] the ion sensitive probe,[8] or the pinhole probe.[9] In Ref. 1, a collection of T_i/T_e measurements from a number of tokamak SOL has been examined for measurements taken before 2010, showing values that range from the lower $T_i/T_e \sim 1$ to the extreme $T_i/T_e \sim 10$, with most of the data falling between 1 and 4. More recent measurements, in HL-2A,[3] in MAST,[2,4] in Alcator C-MOD,[7,8] and in ASDEX Upgrade[6] have confirmed these findings. The ion temperature is therefore usually higher than the electron one in the SOL. Moreover, in Ref. 1, the SOL e-folding lengths for T_e and T_i are shown for different tokamaks, indicating that the electron profile is usually steeper than the ion profile, leading to $\eta_e(=L_n/L_{T_e}) > \eta_i(=L_n/L_{T_i})$. The η_i value has been measured, e.g., during limited discharges in Tore Supra,[10] and during diverted discharges in JFT-2M[11] resulting in $\eta_i < 1$ in both cases.

The numerical simulation of edge turbulence in the presence of ion temperature dynamics has been the subject of numerous studies.[12–20] Ion temperature gradient (ITG) is responsible for the rising of an instability called ITG mode (see, e.g., Ref. 12), which can drive cross-field transport of particles and energy. Moreover, T_i effects have an impact on SOL instabilities that exist in the cold ion limit, such as the ballooning mode (BM) and the drift wave (DW) instabilities. In general, the ratio between the background ion and electron temperature, $\tau = T_{i0}/T_{e0}$, and η_i, is found to be crucial parameter for determining the role of ITG turbulence in the SOL, and of the T_i effects on other instabilities. Zeiler *et al.*[12–15] describe the linear and non-linear transition between resistive ballooning mode (RBM) and ITG-driven turbulence in the tokamak edge by using a gradient-driven flux-tube code,[16] identifying the non-linearly prevailing instability as a function of the gradient scale length and the α_d parameter that represents the ratio between the diamagnetic frequency and the BM growth rate. It is found that at steep gradients the RBM drives turbulence when diamagnetic effects are negligible (small α_d) and it is overpowered by the non-linear drift wave instability for increasing values of α_d. The ITG instability dominates instead at high values of α_d and broad gradients. In a later study,[15] Hallatschek and Zeiler focus on non-locality effects on the transition between RBM and ITG, finding a general quenching of the instability when the turbulence scale length becomes comparable to the gradient scale length (increasing non-locality). Scott *et al.* also developed a suite of numerical tools for the simulation of the SOL turbulence finite ion temperature effects; in particular, the fluid DALF code[17,18] and the gyrofluid GEM code.[18,21] The ITG signature is identified in large and dominant T_i fluctuations associated with a higher ion with respect to electron radial transport.[17]

The goal of the present paper is to improve the understanding of the role of finite ion temperature in SOL turbulence. First, we study T_i effects on the SOL linear instabilities that exist also in the cold ion limit, and we introduce the main properties of the ITG instability. Second, we identify the SOL turbulent regimes based on the instability that drive the non-linear transport as a function of the SOL operational parameters. We show that ITG modes, and, in general, finite ion temperature effects, play a negligible role in limited SOL discharges. The methodology we use to

[a)]Electronic address: annamaria.mosetto@epfl.ch
[b)]Current address: Max-Planck-Institut für Plasmaphysik, D-17491 Greifswald, Germany.

identify the non-linear SOL instability is supported by the analysis of non-linear simulations performed with the GBS code.[22] GBS is a three-dimensional fluid code used to describe the evolution of the plasma density, electric potential, electron and ion parallel velocities, and electron and ion temperatures in the tokamak SOL. The code advances the plasma dynamics as an interplay among the plasma density and energy outflowing from the plasma core, the parallel losses at the limiter plates, and the cross field transport due to turbulence, without separation of equilibrium and fluctuations.

The drift-reduced Braginskii model we use[12] includes the effect of the polarisation drift in the T_i equation that becomes important for $k_y\rho_s \sim 1$ (Refs. 14 and 21). Nevertheless, finite Larmor radius (FLR) effects contained in the stress tensor are neglected, and the electric potential is evaluated at the particle gyrocentre, contrary to gyrofluid models (see, e.g., Ref. 23). We also remark that other effects present in collisionless plasmas, such as trapped particles and wave-particle resonances, are not contained in the Braginskii equations. Therefore, our model does not describe accurately perturbations with a perpendicular wavelength of the order of ρ_i, or where kinetic effects are important. However, for typical limited SOL parameters, turbulence is dominated by modes with perpendicular scales much larger than ρ_i, and kinetic effects are expected to be negligible due to the large collisionality, justifying our model assumptions. The setting, a plasma limited on the high field side at the equatorial midplane, is rather simple, nevertheless allows us to identify the key mechanisms at play in the SOL.

The present paper is organized as follows. In Sec. II, we describe the model we use for the SOL description and its boundary conditions in the presence of hot ions. Ion temperature effects on the linear SOL instabilities are presented in Sec. III. In Sec. IV, we describe estimate of the SOL equilibrium pressure gradient length, then, in Sec. V, we identify the SOL turbulent regimes with hot ions. We discuss the results of non-linear GBS simulations with hot ions and we compare our expectations to the GBS results in Sec. VI Finally, in Sec. VII, we draw our conclusions.

II. THE MODEL

A. The drift-reduced Braginskii equations with hot ions

Our study of plasma turbulence in the SOL is based on the two-fluid, electrostatic, non-linear, drift-reduced Braginskii equations.[24] The fluid approach is justified by the high plasma collisionality in the SOL. We also consider the electrostatic limit, neglecting the ideal branch of the BM. The role of the ideal BM in SOL turbulence is investigated in Ref. 25.

In the drift-reduced limit, we assume for the perpendicular velocities $\mathbf{V}_{\perp i} = \mathbf{V}_{E\times B} + \mathbf{V}_{*i} + \mathbf{V}_{pol}$ and $\mathbf{V}_{\perp e} = \mathbf{V}_{E\times B} + \mathbf{V}_{*e}$, where $\mathbf{V}_{E\times B} = (-\nabla\phi \times \mathbf{b})c/B$ is the $\mathbf{E}\times\mathbf{B}$ drift velocity, $\mathbf{V}_{*e} = -(\mathbf{b}\times\nabla p_e)c/(enB)$ is the electron diamagnetic drift velocity, $\mathbf{V}_{*i} = (\mathbf{b}\times\nabla p_i)c/(enB)$ is the ion diamagnetic drift velocity, and $\mathbf{V}_{pol}$ is the ion polarization velocity (see, e.g., Ref. 13). The equations that describe the evolution of density, n, potential, ϕ, electron parallel velocity, $V_{\parallel e}$, ion parallel velocity, $V_{\parallel i}$, electron temperature, T_e, and ion temperature, T_i are

$$
\begin{aligned}
\frac{\partial n}{\partial t} &= -\frac{R}{\rho_{s0}}[\phi, n] + 2\left[nC(T_e) + T_eC(n) - nC(\phi)\right] \\
&\quad - n\nabla_\parallel V_{\parallel e} - V_{\parallel e}\nabla_\parallel n + \mathcal{D}_n(n) + S_n, \\
\frac{\partial \omega}{\partial t} + \tau\frac{\partial \nabla_\perp^2 T_i}{\partial t} &= -\frac{R}{\rho_{s0}}[\phi,\omega] - \tau\frac{R}{\rho_{s0}}\left[\phi, \nabla_\perp^2 T_i\right] \\
&\quad - V_{\parallel i}\nabla_\parallel\omega - \tau V_{\parallel i}\nabla_\parallel\nabla_\perp^2 T_i \\
&\quad + \left[\nabla_\parallel\left(V_{\parallel i} - V_{\parallel e}\right) + \left(V_{\parallel i} - V_{\parallel e}\right)\frac{\nabla_\parallel n}{n}\right] \\
&\quad + 2\left[\tau C(T_i) + \tau\frac{T_i}{n}C(n) + C(T_e) + \frac{T_e}{n}C(n)\right] \\
&\quad + \frac{1}{3n}C(G_i) + \mathcal{D}_\omega(\omega), \\
\frac{\partial V_{\parallel e}}{\partial t} &= -\frac{R}{\rho_{s0}}\left[\phi, V_{\parallel e}\right] - V_{\parallel e}\nabla_\parallel V_{\parallel e} - \frac{m_i}{m_e}\frac{2}{3}\nabla_\parallel G_e \\
&\quad - \frac{m_i}{m_e}\nu\left(V_{\parallel e} - V_{\parallel i}\right) + \frac{m_i}{m_e}\nabla_\parallel\phi \\
&\quad - \frac{m_i}{m_e}\frac{T_e}{n}\nabla_\parallel n - 1.71\frac{m_i}{m_e}\nabla_\parallel T_e + \mathcal{D}_{V_{\parallel e}}\left(V_{\parallel e}\right), \\
\frac{\partial V_{\parallel i}}{\partial t} &= -\frac{R}{\rho_{s0}}\left[\phi, V_{\parallel i}\right] - V_{\parallel i}\nabla_\parallel V_{\parallel i} - \frac{2}{3}\nabla_\parallel G_i - \nabla_\parallel T_e \\
&\quad - T_e\frac{\nabla_\parallel n}{n} - \tau\nabla_\parallel T_i - \tau T_i\frac{\nabla_\parallel n}{n} + \mathcal{D}_{V_{\parallel i}}\left(V_{\parallel i}\right), \\
\frac{\partial T_e}{\partial t} &= -\frac{R}{\rho_{s0}}[\phi, T_e] - V_{\parallel e}\nabla_\parallel T_e \\
&\quad + \frac{4}{3}\left[\frac{7}{2}T_eC(T_e) + \frac{T_e^2}{n}C(n) - T_eC(\phi)\right] \\
&\quad + \frac{2}{3}\left\{T_e\left[0.71\nabla_\parallel V_{\parallel i} - 1.71\nabla_\parallel V_{\parallel e}\right]\right. \\
&\quad \left. + 0.71T_e\left(V_{\parallel i} - V_{\parallel e}\right)\frac{\nabla_\parallel n}{n}\right\} \\
&\quad + \mathcal{D}_{T_e}(T_e) + \mathcal{D}_{T_e}^{\parallel}(T_e) + S_{T_e}, \\
\frac{\partial T_i}{\partial t} &= -\frac{R}{\rho_{s0}}[\phi, T_i] + \frac{4T_i}{3}\left[C(T_e) + \frac{T_e}{n}C(n)\right] \\
&\quad - \frac{4}{3}T_iC(\phi) + \frac{2}{3}T_i\left(V_{\parallel i} - V_{\parallel e}\right)\frac{\nabla_\parallel n}{n} \\
&\quad - \frac{2}{3}T_i\nabla_\parallel V_{\parallel e} - V_{\parallel i}\nabla_\parallel T_i - \tau\frac{10}{3}T_iC(T_i) \\
&\quad + \mathcal{D}_{T_i}(T_i) + S_{T_i}.
\end{aligned} \tag{1}
$$

In Eq. (1), we introduce the vorticity, $\omega = \nabla_\perp^2\phi$, the adimensionalized resistivity, $\nu = e^2nR/(m_i\sigma_\parallel c_{s0})$, being $\sigma_\parallel = 1.96ne^2\tau_e/m_e$ the parallel Spitzer conductivity, the ion to electron background temperature ratio, $\tau = T_{i0}/T_{e0}$, and R, the tokamak major radius. The vorticity equation, second equation in Eq. (1), is derived by applying the Boussinesq approximation, namely

$$\nabla\cdot\frac{nc}{B\Omega_{ci}}\frac{d}{dt}\left(\mathbf{E}_\perp - \frac{\nabla_\perp p_i}{en}\right) \simeq \frac{nc}{B\Omega_{ci}}\frac{d}{dt}\left(-\nabla_\perp^2\phi - \frac{\nabla_\perp^2 T_i}{e}\right). \tag{2}$$

Despite the fact that the detailed evaluation of the divergence of the polarization drift has been carried out,[26,27] the

Boussinesq approximation is widely used in the numerical studies of drift-reduced models as it makes the solution of the equation considerably simpler. A number of studies have been performed to evaluate the impact of this approximation and they can be found, for example, in Refs. 28–30. The source terms S_n, S_{T_e}, and S_{T_i} mimic the flow of plasma into the SOL through the last closed flux surface. The terms $\mathcal{D}_f(f)$ represent small perpendicular diffusion added for numerical reasons. For the gyroviscous part of the stress tensor,[31] represented by G_e and G_i, we use the expressions derived in Ref. 22. The Poisson brackets are expressed as $[f, g] = \mathbf{b} \cdot (\nabla f \times \nabla g)$, where $\mathbf{b}$ is the unit magnetic field vector and the curvature operator is $C(f) = RB/2\, [\nabla \times (\mathbf{b}/B)] \cdot \nabla f$. In Eq. (1), and in the remainder of the present paper, we normalize n to the reference density n_0, ϕ to T_{e0}/e, T_e to the reference electron temperature T_{e0}, T_i to the reference ion temperature T_{i0}, $V_{\|e}$ and $V_{\|i}$ to $c_{s0} = \sqrt{T_{e0}/m_i}$ (and therefore c_s to c_{s0}), and time t to R/c_{s0}. Lengths in the perpendicular direction are adimensionalized to $\rho_{s0} = c_{s0}/\Omega_{ci}$ and in the parallel direction to R.

For simplicity, we consider the system of Eq. (1) in s-α circular geometry[32] with a toroidal limiter positioned on the high field side equatorial midplane of the device. In this geometry, operators are computed in the $a/R \to 0$ limit (a is the tokamak minor radius) and we neglect magnetic shear. Therefore, the Poisson brackets reduce to $[f, g] = \partial_y f \partial_x g - \partial_x f \partial_y g$, where x is the flux coordinate and corresponds, in a circular magnetic flux surface configuration, to the radial direction, while y is the coordinate perpendicular to x and $\mathbf{B}$. In the $a/R \to 0$ limit, the plane (x, y) coincides with the poloidal plane and, as a consequence, $y = a\theta$, where $0 < \theta < 2\pi$ is the poloidal angle, with $\theta = 0$ and $\theta = 2\pi$ at the outer midplane, where the toroidal limiter is located. Moreover, the expression of the curvature operator is $C(f) = \sin\theta \partial_x f + \cos\theta \partial_y f$. The perpendicular Laplace operator is $\nabla^2_\perp f = \partial^2_x f + \partial^2_y f$, and the parallel gradient reads as $\nabla_\| f = \partial_z f$, where z is the direction parallel to the field lines, $0 < z < 2\pi q$. The system of Eq. (1) is completed by an appropriate set of boundary conditions at the magnetic presheath (MP) entrance, derived in Sec. II B.

B. Boundary conditions at the magnetic presheath entrance

The boundary conditions for the drift-reduced Braginskii equations at the MP entrance have been derived in the cold ion limit in Ref. 33. In the following, we extend the study presented in Ref. 33 to the $T_i \neq 0$ case. These boundary conditions have to be applied at $\theta = 0$ and $\theta = 2\pi$, where the plasma touches the limiter and spontaneously generates a thin layer contiguous to the wall, the so-called sheath, where quasi-neutrality and the drift approximations are broken. In particular, when the magnetic field is oblique with respect to an absorbing wall, three regions can be identified at the plasma-wall transition: the collisional presheath (CP), the MP, and the Debye sheath (DS). They are characterized by very different length scales. In the CP, whose size scales with the ion mean free path, λ_{mfp}, the ions are magnetized and the plasma is quasi-neutral. At the MP entrance, the ions reach the sound speed. The width of the MP scales as ρ_s. In this region, the plasma is still quasi-neutral, but ions are demagnetized due to the high electric field. The DS scales as the Debye length, λ_D, being in this region quasi-neutrality violated. Since quasi-neutrality is violated in the DS and the ion drift approximation loses its validity in the MP, the validity of the drift-reduced Braginskii equations stops at the MP entrance, where boundary conditions that properly describe the sheath physics have to be applied.

The dynamics at the plasma-wall transition is described by using the same coordinate system introduced in Sec. II A. We also define the coordinate $s = y\cos\alpha + z\sin\alpha$, normal to the wall, being α the angle of incidence of the magnetic field to the wall. The s coordinate is adimensionalized to ρ_{s0}. The magnetic field is assumed constant.

To describe the steady-state dynamics of the plasma in the CP, we use the ion continuity, the parallel ion velocity, and the electron parallel velocity equations. We consider plasma gradients in the x direction with an ordering $\epsilon = \rho_s/L_n \sim \rho_s/L_T \sim \rho_s/L_\phi \ll 1$. Moreover, we neglect ion FLR effects; in particular, we assume that the particles are lost to the wall when their gyrocenters are.

The steady-state ion continuity equation reads as $\nabla \cdot (n\mathbf{V}_i) = S_{p,i}$, where $S_{p,i}$ represents the ion density source and the perpendicular components of V_i ($V_{x,i}$ and $V_{y,i}$) are computed by neglecting $\mathbf{V}_{pol}$, as in Ref. 33, therefore retaining only 0th order terms in $(1/\omega_i)d/dt$, and assuming $\partial_s T_i = 0$

$$V_{x,i} = V_{x,Ei} + V_{x,*i} = -\partial_y\phi - \tau\frac{T_i}{n}\partial_y n, \tag{3}$$

$$V_{y,i} = V_{y,Ei} + V_{y,*i} = \partial_x\phi + \tau\frac{T_i}{n}\partial_x n. \tag{4}$$

The validity of the isothermal ion assumption as well as $\partial_s T_e = 0$, used later, are discussed in Appendix. The first terms on the right-hand side of Eqs. (3) and (4) represent the $\mathbf{E} \times \mathbf{B}$ drift contribution to the ion velocity, while the second terms are due to the diamagnetic drift. Using the relation $V_{s,i} = V_{\|,i}\sin\alpha + V_{y,i}\cos\alpha$, we obtain, for the ion continuity equation

$$\begin{aligned}\nabla \cdot (n\mathbf{V}_i) &= n\partial_x V_{x,Ei} + n\cos\alpha\partial_s V_{y,Ei} + V_{s,i}\partial_s n \\ &\quad - V_{y,*i}\cos\alpha\partial_s n + n\sin\alpha\partial_s V_{\|i} + V_{x,Ei}\partial_x n = S_{p,i}.\end{aligned} \tag{5}$$

The sum of the first and the second terms on the right hand side vanishes since $n\cos\alpha\partial_s V_{y,Ei} = n\cos\alpha\partial_s\partial_x\phi = -n\partial_x V_{x,Ei}$. The third and fourth terms are gathered together by introducing $V'_{s,i} = V_{s,i} - V_{y,*i}\cos\alpha$. We remark that the diamagnetic contribution appearing in the fourth term cancels out with the identical term appearing in the definition of $V_{s,i}$, as expected, since the ion diamagnetic flux is divergence free. For the sixth term, we have $V_{x,Ei}\partial_x n = -\partial_x n\cos\alpha\partial_s\phi$. Accordingly, Eq. (5) is simplified as

$$V'_{s,i}\partial_s n + n\sin\alpha\partial_s V_{\|,i} - \partial_x n\cos\alpha\partial_s\phi = S_{p,i}, \tag{6}$$

which constitutes the form of the ion continuity equation that we consider for our analysis.

The steady state ion momentum equation reads as

$$n(\boldsymbol{V}_i \cdot \nabla)\boldsymbol{V}_i = n\mathbf{E} + n\mathbf{V}_i \times \mathbf{b} - \nabla p_i + \boldsymbol{S}_{m_i}, \quad (7)$$

where $\boldsymbol{S}_{m_i}$ represents the ion momentum source. For sake of simplicity, we write the total derivative $d_t = \partial_t + (\boldsymbol{V}_{\parallel i} + \boldsymbol{V}_{E\times B}) \cdot \nabla$, by neglecting the polarization drift, since smaller than the other contributions. We note that the diamagnetic velocity does not appear in the convective derivative due to the diamagnetic cancellation.[12] The parallel component of Eq. (7) can be written therefore as

$$n(V'_{si}\partial_s + V_{xi}\partial_x)V_{\parallel i} = -n\partial_s\phi \sin\alpha - \tau T_i \partial_s n \sin\alpha + S_{\parallel m_i}. \quad (8)$$

Substituting Eq. (3) into Eq. (8), we find

$$nV'_{si}\partial_s V_{\parallel i} + \sin\alpha(n\partial_s\phi + \tau T_i \partial_s n) - n\partial_x V_{\parallel i}\cos\alpha\partial_s\phi = S_{\parallel m_i}, \quad (9)$$

where the third term represents the ion pressure contribution. Finally, the momentum equation for the electrons reads as

$$n(\boldsymbol{V}_e \cdot \nabla)\boldsymbol{V}_e = -\mu(n\boldsymbol{E} + n\boldsymbol{V}_e \times \boldsymbol{b} + \nabla p_e) + \boldsymbol{S}_{m_e}, \quad (10)$$

where $\boldsymbol{S}_{m_e}$ is the electron momentum source, and $\mu = m_i/m_e$. Equation (10) is simplified assuming $\mu \gg 1$ and isothermal electrons in the CP, i.e., $\partial_s T_e = 0$. The parallel component of Eq. (10) reads, therefore, as

$$\mu \sin\alpha T_e \partial_s n - \mu \sin\alpha n \partial_s \phi = S_{\parallel m_e}. \quad (11)$$

Equations (6), (9), and (11) can be written in the form of a system of linear equations, $\boldsymbol{MX} = \boldsymbol{S}$, where $\boldsymbol{X} = [\partial_s n, \partial_s V_{\parallel i}, \partial_s\phi]$, $\boldsymbol{S} = [S_{p,i}, S_{\parallel m_i}, S_{\parallel m_e}]$, and

$$M = \begin{pmatrix} V'_{si} & n\sin\alpha & -\partial_x n\cos\alpha \\ \sin\alpha\tau T_i & nV'_{si} & n(\sin\alpha - \partial_x V_{\parallel i}\cos\alpha) \\ \mu\sin\alpha T_e & 0 & -\mu n\sin\alpha \end{pmatrix}. \quad (12)$$

In the $T_i = 0$ limit, we retrieve the system of equations reported in Eq. (11) of Ref. 33. When T_i dynamics is included, a new term, due to the ion pressure, appears in Eq. (12) and $V_{s,i}$ is redefined as $V'_{s,i}$, to take into account the presence of the ion diamagnetic drift. Equations (6), (9), and (11) are valid in the CP, up to the MP entrance. In the CP, the source terms are responsible for the small plasma gradients. Approaching the MP entrance, gradients become large, while the intensity of the source terms remains the same as in the main SOL plasma. Non-zero gradients in the MP exist, therefore, with negligible sources, leading to $\boldsymbol{MX} \simeq 0$ to define the location of the MP entrance. This condition requires that $\det M = 0$ is satisfied, resulting in

$$V'_{s,i} = \sqrt{T_e}\sin\alpha\left[\theta_n \pm \sqrt{\left(1 + \tau\frac{T_i}{T_e}\right) + \theta_n^2 - \frac{\partial_x V_{\parallel i}}{\tan\alpha}}\right], \quad (13)$$

where

$$\theta_n = \frac{\sqrt{T_e}}{2\tan\alpha}\frac{\partial_x n}{n} \quad (14)$$

has been defined. In Eq. (13) and in the following, the upper sign is for the case when the coordinate s increases towards the wall and the lower sign is for the opposite case, corresponding in our setting to the upper and lower sides of the limiter, respectively. Recalling $V_{s,i} = V_{\parallel,i}\sin\alpha + V_{y,i}\cos\alpha$ and $V_{y,i} \sim \mathrm{O}(\epsilon)$, from Eq. (13) we have $\partial_x V_{\parallel i} = \partial_x\sqrt{T_e} + \mathrm{O}(\epsilon^2)$. We can, therefore, write Eq. (13) as

$$V'_{s,i} = \sqrt{T_e}\sin\alpha\left[\theta_n \pm \sqrt{\left(1 + \tau\frac{T_i}{T_e}\right) + \theta_n^2 - \theta_T}\right], \quad (15)$$

where

$$\theta_T = \frac{\sqrt{T_e}}{2\tan\alpha}\frac{\partial_x T_e}{T_e}. \quad (16)$$

In the following, we neglect terms of order $\mathrm{O}(\epsilon^2)$ and higher. By introducing $F_T = 1 + \tau T_i/T_e$, the condition for $V'_{s,i}$ becomes therefore

$$V'_{s,i} = \sqrt{T_e}\sin\alpha\left[\theta_n \pm \left(\sqrt{F_T} - \frac{1}{2\sqrt{F_T}}\theta_T\right)\right], \quad (17)$$

and the boundary conditions for $V_{\parallel i}$ are derived from Eq. (15), using the relation

$$V_{\parallel i}\sin\alpha = V_{s,i} - V_{y,i}\cos\alpha. \quad (18)$$

In the evaluation of $V_{\parallel i}$, we remark that the ion diamagnetic contributions in $V_{y,i}$ and in $V'_{s,i}$ cancel out, so that only $V_{y,Ei}$ appears in Eq. (19). The boundary condition for $V_{\parallel i}$ reads as

$$V_{\parallel i} = \sqrt{T_e}\left(\theta_n \pm \sqrt{F_T} \mp \frac{1}{2\sqrt{F_T}}\theta_T - \frac{2\phi}{T_e}\theta_\phi\right), \quad (19)$$

where

$$\theta_\phi = \frac{\sqrt{T_e}}{2\tan\alpha}\frac{\partial_x\phi}{\phi}, \quad (20)$$

and, therefore, the fourth term in Eq. (19) is the contribution to $V_{\parallel i}$ of the $\boldsymbol{E} \times \boldsymbol{B}$ drift. The boundary conditions for the density n and the potential ϕ can be derived by solving for $\det M = 0$, the linear system of equations $\boldsymbol{MX} = 0$, obtaining

$$\partial_s n = \frac{n}{T_e}\partial_s\phi \quad (21)$$

and

$$\partial_s\phi = -\frac{V'_{s,i}\partial_s V_{\parallel i}}{\sin\alpha F_T - \cos\alpha\partial_x V_{\parallel i}}. \quad (22)$$

Keeping only first order terms in ϵ, Eqs. (21) and (22) can be written as

$$\partial_s n = -\frac{n}{\sqrt{T_e}}\left(\pm\frac{1}{\sqrt{F_T}} + \frac{\theta_n}{F_T} \pm \frac{\theta_T}{2F_T^{3/2}}\right)\partial_s V_{\parallel i}, \quad (23)$$

$$\partial_s\phi = -\sqrt{T_e}\left(\pm\frac{1}{\sqrt{F_T}} + \frac{\theta_n}{F_T} \pm \frac{\theta_T}{2F_T^{3/2}}\right)\partial_s V_{\parallel i}. \quad (24)$$

The boundary condition for the vorticity is derived from the boundary condition for ϕ

$$\omega = \nabla_\perp^2 \phi = \partial_y^2 \phi + \partial_x^2 \phi = \partial_y^2 \phi + \mathrm{O}(\epsilon^2), \tag{25}$$

where ϵ^2 terms are neglected. Moreover, we can use $\partial_y^2 \phi = \cos^2\alpha \partial_s^2 \phi$, where we estimate $\partial_s^2 \phi$ at the MP entrance, deriving Eq. (22) with respect to s. Finally, neglecting second order terms in ϵ, and substituting $V'_{s,i}$ with its expression in Eq. (17), we obtain

$$\omega = -\cos^2\alpha \left[\left(\frac{1}{F_T} + \frac{1}{F_T^2}\theta_T \right) (\partial_s V_{\parallel i})^2 + \sqrt{T_e} \left(\pm \frac{1}{\sqrt{F_T}} + \frac{\theta_n}{F_T} \pm \frac{\theta_T}{2F_T^{3/2}} \right) \partial_s^2 V_{\parallel i} \right]. \tag{26}$$

The $V_{\parallel e}$ boundary condition is derived by using a detailed kinetic treatment of the electron dynamics in the sheath region, including gradients in the x direction (see Ref. 33 and references therein), and reads as

$$V_{\parallel e} = \sqrt{T_e} \left(\pm \exp(\Lambda - \eta_m) - \frac{2\phi}{T_e}\theta_\phi + 2(\theta_n + \theta_T) \right), \tag{27}$$

where $\eta_m = (\phi_{MPE} - \phi_{wall})/T_e$, being $\phi_{MPE} - \phi_{wall}$ the potential drop between the MP entrance and the wall, and $\Lambda = \log\sqrt{\mu/2\pi}$. Equation (27) is valid in the limit $\rho_e \ll \lambda_D$, i.e., when electrons are magnetized all the way to the wall. The case $\rho_e \gtrsim \lambda_D$ leads to complex electron trajectories in the DS, preventing us from obtaining a simple expression of the $V_{\parallel e}$ boundary conditions, such as the one in Eq. (27).

Equations (19), (27), (23), (24), and (26) are the boundary conditions for $V_{\parallel i}$, $V_{\parallel e}$, n, ϕ, and ω at the magnetic presheath entrance. Together with the conditions of isothermal ions and electron ($\partial_s T_e = 0$ and $\partial_s T_i = 0$), they form the set of boundary conditions, generalized to the case of hot ions, that can be applied to the drift-reduced Braginskii equations. In the $\tau = 0$ limit, we retrieve Eqs. (33)–(38) of Ref. 33. We note that the s derivative can be approximated by the derivative taken along the y direction.

In the radial direction, the SOL boundaries correspond to the tokamak vessel wall and to the separatrix. Since most of the particles are lost at the limiter plates, preventing them from reaching the vessel wall, the conditions applied to the outer edge of the simulation domain do not significantly impact the turbulence. *Ad hoc* boundary conditions are therefore applied at this location. On the other hand, at the separatrix, the hot plasma reaches the SOL from the core. In GBS, a particle and heat source mimic the plasma outflow from the core. This source is located at a finite distance from the inner boundary of the computational domain. The region of the domain between the source and the inner boundary acts as a buffer region and it has not to be taken into account for turbulence analysis. Therefore, also at the inner boundary, *ad hoc* boundary conditions are used as their impact on turbulence properties is not significant.

III. THE LINEAR INSTABILITIES

In this section, we present the main linear SOL instabilities in the presence of hot ions, focusing on the electrostatic limit. In Ref. 34, the resistive and inertial branches of the drift wave (RDW and InDW) and of the ballooning mode (RBM and InBM) are described in the cold ion limit, identifying the instability with the largest growth rate as a function of the SOL parameters. In the following, we first describe the impact of the hot ion dynamics on the fore-mentioned instabilities. We then introduce a mode driven unstable by the presence of the ion temperature gradient, the so-called ITG instability, with its slab (sITG) and toroidal (tITG) branches.

The linear analysis is based on the following system of equations, obtained from Eq. (1), by assuming constant background radial gradients of n, T_e, and T_i (L_n, L_{Te}, and L_{Ti}), while neglecting the background gradient of ϕ

$$\begin{aligned}
\gamma n &= \frac{R}{L_n}\frac{\partial \phi}{\partial y} + 2\hat{C}(n - \phi + T_e) - \nabla_\parallel V_{\parallel e}, \\
\gamma \nabla_\perp^2 \phi + \tau\gamma\nabla_\perp^2 T_i &= 2\left[\hat{C}(T_e + n) + \tau\hat{C}(T_i + n)\right] + \left(\nabla_\parallel V_{\parallel i} - \nabla_\parallel V_{\parallel e}\right), \\
\gamma V_{\parallel e} &= -\frac{m_i}{m_e}\nabla_\parallel(n - \phi + 1.71 T_e) + \frac{m_i}{m_e}\nu\left(V_{\parallel i} - V_{\parallel e}\right), \\
\gamma V_{\parallel i} &= -\nabla_\parallel[n + T_e + \tau(n + T_i)], \\
\gamma T_e &= \frac{R}{L_{Te}}\frac{\partial \phi}{\partial y} + \frac{4}{3}\hat{C}\left(n - \phi + \frac{7}{2}T_e\right) + \frac{2}{3}0.71\left(\nabla_\parallel V_{\parallel i} - \nabla_\parallel V_{\parallel e}\right) - \frac{2}{3}\nabla_\parallel V_{\parallel e}, \\
\gamma T_i &= \frac{R}{L_{Ti}}\frac{\partial \phi}{\partial y} + \frac{4}{3}\hat{C}(n - \phi + T_e) - \frac{2}{3}\nabla_\parallel V_{\parallel e} - \frac{10}{3}\tau\hat{C}(T_i),
\end{aligned} \tag{28}$$

where we ignore the radial dependence of the unstable modes assuming $k_x \ll k_y$. Therefore, the curvature operator reads as $\hat{C} = \cos\theta\partial_y$, and the Laplacian operator reduces to $\nabla_\perp^2 = \partial_y^2$.

A. Drift waves instability

The linear DW instability has been described in the cold ion limit in Ref. 34. In the following, we describe the DW instability including finite T_i effects, simplifying Eq. (28) by neglecting the sound wave coupling, i.e., by assuming $\gamma \gg k_\parallel$, the ballooning drive, the compressibility terms in the continuity and temperature equations, and finite β effects. Under these assumptions, if we furthermore assume $\partial_y \to ik_y$ and $\nabla_\parallel \to ik_\parallel$, we reduce Eq. (28) to an algebraic dispersion relation in the form

$$\gamma^3 a_{DW} + \gamma^2 b_{DW} + \gamma c_{DW} + d_{DW} = 0, \tag{29}$$

where the coefficients are

$$
\begin{aligned}
a_{DW} &= -\frac{m_e}{m_i}k_y^2, \\
b_{DW} &= -k_y^2\left(\nu + i\tau\eta_i\frac{m_e}{m_i}\omega_*\right), \\
c_{DW} &= -k_\parallel^2\left(1+2.95k_y^2\right) - \tau k_y^2\left(i\eta_i\nu\omega_* + \frac{2}{3}k_\parallel^2\right), \\
d_{DW} &= ik_\parallel^2\omega_*(1+1.71\eta_e) + i\tau k_\parallel^2\omega_* k_y^2 \\
&\quad\times\left[\frac{2}{3}(1+1.71\eta_e) - 2.95\eta_i\right],
\end{aligned} \tag{30}
$$

where $\omega_* = k_y R/L_n$, $\eta_e = L_n/L_{T_e}$, and $\eta_i = L_n/L_{T_i}$. First, we note that in the limit $\tau \to 0$, we retrieve the dispersion relation of the RDW, if $m_e/m_i \to 0$, and of the InDW, if $\nu \to 0$, as presented in Ref. 35. Second, we observe that, in the resistive limit, Eq. (29) can be rewritten by using exclusively the following parameters: $\breve{\gamma} = \gamma/[R/L_n(1+1.71\eta_e)]$, $k_{\parallel*}^2 = k_\parallel^2/[k_y^2\nu\omega_*(1+1.71\eta_e)]$, k_y, $\eta_{i*} = \eta_i/(1+1.71\eta_e)$, and τ. For $\tau = 0$, we retrieve the cold ion limit results: peak growth rate at $k_y \simeq 0.57$ and $k_{\parallel*} \simeq 0.56$, with $\breve{\gamma} = \breve{\gamma}_0 \simeq 0.085$ (see Ref. 35). In Fig. 1(a), we show $\breve{\gamma}/\breve{\gamma}_0$, solution of Eq. (29), in the resistive limit, maximized over $k_{\parallel*}$ and k_y, as a function of τ and η_{i*}. The maximum growth rate decreases with η_{i*} and this effect is more evident at large τ. The η_{i*} terms in the d_{DW} and c_{DW} coefficients of Eq. (30) are responsible for the decrease of the growth rate for $0.5 \lesssim \eta_i \lesssim 1$, and for $\eta_{i*} \gtrsim 1$, respectively. Similarly, in the inertial limit, Eq. (29) can be rewritten by introducing $k_{\parallel*}^2 = k_\parallel^2/[k_y^2\omega_*^2 m_e/m_i (1+1.71\eta_e)^2]$, and $\eta_{i*} = \eta_i/(1+1.71\eta_e)$. For $\tau = 0$, we retrieve the cold ion limit results: peak growth rate $\breve{\gamma} = \breve{\gamma}_0 \simeq 0.17$ at $k_y \simeq 0.57$ and $k_{\parallel*} \simeq 0.6$ (see Ref. 35).

In Fig. 1(b), we show $\breve{\gamma}/\breve{\gamma}_0$, solution of Eq. (29), in the inertial limit, maximized over $k_{\parallel*}$ and k_y, as a function of τ and η_{i*}. As in the resistive limit, the maximum growth rate decreases with η_{i*} and this effect is more evident at large τ. Moreover, as in the resistive limit, the η_{i*} term in the d_{DW} coefficient of Eq. (29) is responsible for the decrease of the growth rate at $0.5 \lesssim \eta_i \lesssim 1$, while the η_{i*} term in b_{DW} reduces the growth rate at $\eta_{i*} \gtrsim 1$. In general, the T_i dynamics tends to increase the DW growth rate for $\eta_{i*} \lesssim 0.5$ and for typical τ values in experiments the growth rate is about 5 times larger than in the cold ion limit.

B. Ballooning modes

Here, we extend the cold ion description of the BM of Ref. 34 to include finite ion temperature effects. In the following, we describe the BM instability with hot ion dynamics. We simplify Eq. (28) by neglecting the coupling with sound waves, i.e., $\gamma \gg k_\parallel$, and compressibility terms in the continuity and temperature equations. Moreover, $\nabla_\parallel$ terms in the density and temperature equations, as well as the diamagnetic terms in Ohm's law are neglected, in order to avoid the coupling with DW. Finally, we ignore finite β effects. Under these assumptions, imposing $\partial_y \to ik_y$ and $\nabla_\parallel \to ik_\parallel$, we reduce Eq. (28) to a dispersion relation in the form of a third-order algebraic equation

$$\gamma^3 a_{BM} + \gamma^2 b_{BM} + \gamma c_{BM} + d_{BM} = 0, \tag{31}$$

where

$$
\begin{aligned}
a_{BM} &= k_y^2\frac{m_e}{m_i}, \\
b_{BM} &= k_y^2\nu + ik_y^2\tau\omega_*\eta_i\frac{m_e}{m_i}, \\
c_{BM} &= ik_y^2\tau\omega_*\eta_i\nu - \omega_\kappa\omega_*[1+\eta_e+\tau(1+\eta_i)]\frac{m_e}{m_i} + k_\parallel^2, \\
d_{BM} &= -\omega_\kappa\omega_*[1+\eta_e+\tau(1+\eta_i)]\nu,
\end{aligned} \tag{32}
$$

being $\omega_\kappa = 2k_y\cos\theta$ the frequency associated with the curvature and the gradient of the magnetic field. Equation (31) reduces to the results of Ref. 34, for $\tau = 0$. In the limit $k_\parallel/k_y \to 0$, the maximum growth rate of the BM is attained, $\gamma_B^{max} = \sqrt{2R/L_n(1+\tau+\eta_e+\tau\eta_i)}$, which is larger than the cold ion growth rate because of the presence of the $(\tau\eta_i + \tau)$ term. Finite values of $k_\parallel/k_y$ reduce the growth rate. This effect is ascribed to the $k_\parallel^2$ term in the c_{BM} coefficient of Eq. (32). Similar to what observed in Ref. 34, we find that the

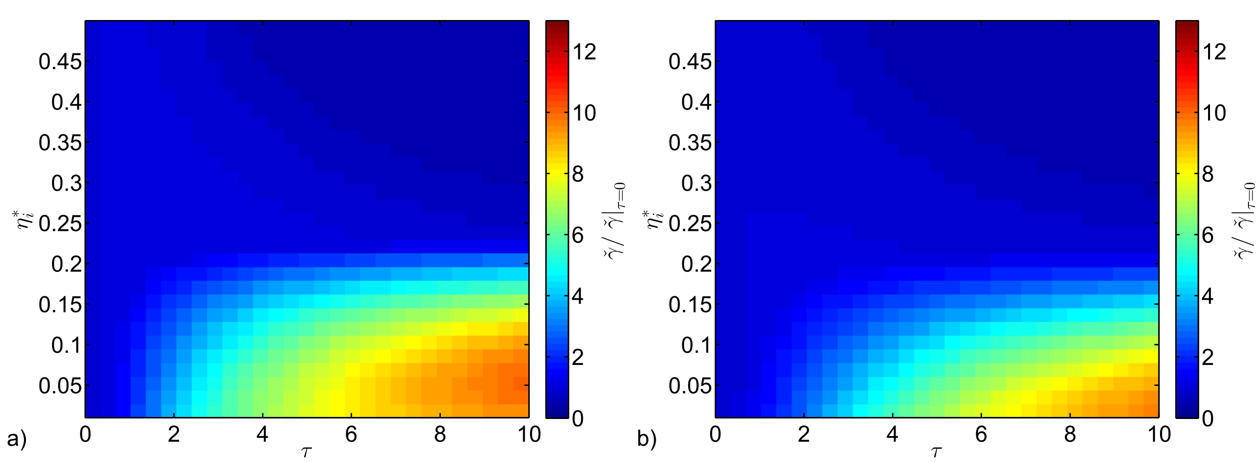

FIG. 1. Maximum $\breve{\gamma}/\breve{\gamma}|_{\tau=0}$, solution of the DW dispersion relation, Eq. (29), in the resistive (a) and in the inertial (b) limits, respectively.

BMs are stabilized for $k_y < k_y^{min}$, where $k_y^{min} = k_\parallel/\sqrt{\gamma_B^{max}\nu}$ for the RBM, and $k_y^{min} = k_\parallel\sqrt{m_i}/(\gamma_B^{max}\sqrt{m_e})$ for the InBM.

We use the linear solver described in Ref. 34 to determine the eigenfunctions of system (28), simplified according to the BM assumptions previously listed (we point out that we preserve the dependence of the eigenfunctions on the parallel coordinate). In Figs. 2(a) and 2(b), we show γ/γ_B^{max}, solution of the BM version of Eq. (28), maximized over k_y, with $q=4$, in the resistive ($\nu=0.1$) and inertial ($m_e/m_i=1/200$) limits, respectively. For both RBM and InBM, the reduction of the growth rate observed at high η_i is due to finite $k_\parallel$ effects. In fact, at large η_i, γ peaks at low k_y, where the term $k_\parallel^2$ in the c_{BM} coefficient of Eq. (32) becomes larger, therefore, reducing γ with respect to γ_B^{max}. We remark that, for both RBM and InBM, the k_y corresponding to the maximum growth rate is large at low R/L_n, since k_y^{min} is a decreasing function of R/L_n.

Finally, stemming from linear calculation (not shown) performed with τ ranging from 1 to 4, we observe that the BM growth rate decreases with τ, with respect to γ_B^{max}, due to the term proportional to τ in the b_{BM} coefficient of Eq. (31), for the InBM, and due to the first term in the c_{BM} coefficient of Eq. (31), for the RBM. To summarize, the T_i dynamics tends to decrease the BM growth rate, with respect to γ_B^{max}, for increasing values of η_i and τ.

C. Ion temperature gradient instability

The presence of an ion temperature gradient can lead to the ITG instability, which develops in two branches, the sITG and the tITG. We can derive a simple dispersion relation that includes both branches of the ITG instability, within the hypothesis of isothermal and adiabatic electrons, from Eq. (28), with $\partial_y \to ik_y$, and $\nabla_\parallel \to ik_\parallel$, obtaining the following dispersion relation:

$$a_{ITG}\gamma^3 + b_{ITG}\gamma^2 + c_{ITG}\gamma + d_{ITG} = 0, \tag{33}$$

where

$$\begin{aligned} a_{ITG} &= 1 + k_y^2\left(1+\frac{2}{3}\tau\right),\\ b_{ITG} &= i\left\{\omega_*\left[-1+k_y^2\tau\left(\eta_i-\frac{2}{3}\right)\right]+\omega_\kappa\left[1+\frac{5}{3}\tau\left(2+k_y^2\right)\right]\right\},\\ c_{ITG} &= k_\parallel^2\left(1+\frac{5}{3}\tau\right)+\omega_\kappa\tau\left[\omega_*\left(\frac{7}{3}-\eta_i\right)-\frac{5}{3}\omega_\kappa(1+\tau)\right],\\ d_{ITG} &= ik_\parallel^2\tau\left[\omega_*\left(\eta_i-\frac{2}{3}\right)+\frac{5}{3}\omega_\kappa(1+\tau)\right], \end{aligned} \tag{34}$$

which describes both the slab and toroidal branches of the ITG instability, analyzed below.

It is the parallel compression of the plasma, that in a homogeneous plasma simply develops a parallel sound wave, that in a inhomogeneous plasma drives the sITG instability. An estimate of the peak value of γ for the ITG instability, and of the corresponding $k_\parallel$, can be found by simplifying the dispersion relation Eq. (33). Beside neglecting ω_κ in Eq. (33) and assuming $\nabla_\parallel j_\parallel = 0$, we suppose $\omega_* \ll \gamma$ and $\eta_i \gg 1$. The ITG dispersion relation becomes

$$\hat{\gamma}^3 + \left(1+\frac{5}{3}\tau\right)k_{\parallel *}^2\hat{\gamma} + ik_{\parallel *}^2\tau = 0, \tag{35}$$

where $\hat{\gamma} = \gamma/(\omega_*\eta_i)$ and $k_{\parallel *} = k_\parallel/(\omega_*\eta_i)$. Therefore, the peak growth rate can be written as $\gamma_{max} \simeq g(\tau)\omega_*\eta_i$, and it occurs at $k_\parallel \simeq f(\tau)\omega_*\eta_i$. It is found that $g(\tau)$ is an increasing function of τ, while $f(\tau)$ decreases with τ.

The tITG instability is a curvature driven instability, similar to the BM and contrary to the sITG, due to the presence of an ion temperature gradient in the plasma. The instability mechanism is similar to one of the BMs,[12] with the drive provided by T_i fluctuations. While a $\pi/2$ shift between n and ϕ characterizes the BM instability, in case of tITG, a $\pi/2$ shift between T_i and ϕ is maintained, and electrons can be adiabatic. With respect to the sITG, the tITG branch exists at $k_\parallel = 0$. We can retrieve a simple dispersion relation of the tITG starting from Eq. (33), by neglecting the $\nabla_\parallel^2$ terms

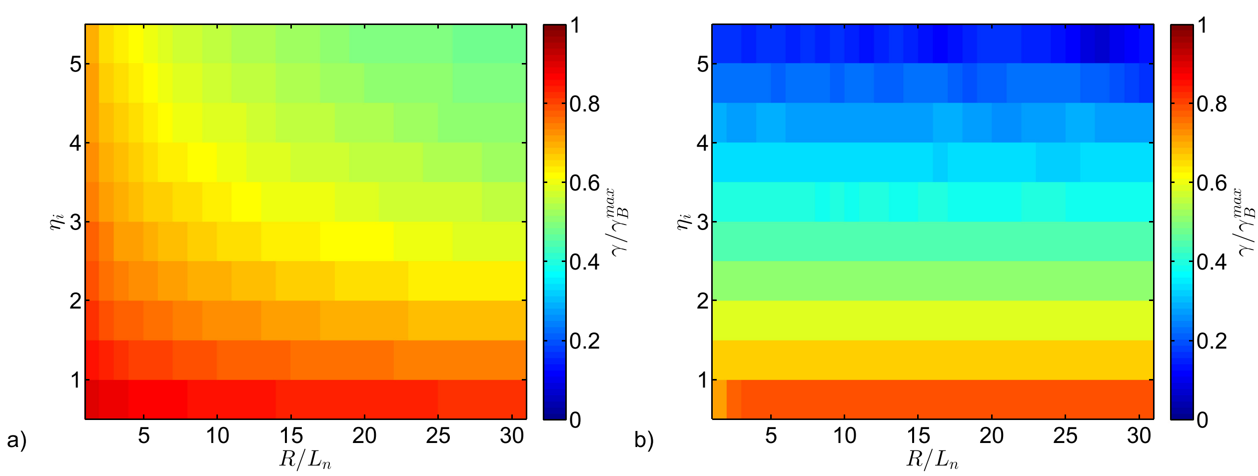

FIG. 2. Growth rate of the RBM for $\nu = 0.1$, $m_e/m_i \to 0$ (a), and of the InBM for $\nu \to 0$, $m_e/m_i = 1/200$ (b), $\eta_e = 0.79$. It is $\tau = 1$.

$$\gamma^2\left[1+k_\perp^2\left(1+\tau\frac{2}{3}\right)\right]+\gamma i\left[-\omega_*+\omega_\kappa\left(1+\frac{10}{3}\tau\right)\right.$$
$$\left.+k_\perp^2\tau\left(\omega_*\left(\eta_i-\frac{2}{3}\right)+\frac{5}{3}\omega_\kappa\right)\right]$$
$$-\omega_\kappa\tau\left[\omega_*\left(\eta_i-\frac{7}{3}\right)+\frac{5}{3}\omega_\kappa(1+\tau)\right]. \quad (36)$$

The largest growth rate is attained by the modes for which the linear term of Eq. (36) is small.[14] Since $\omega_\kappa/\omega_* \sim L_n/R \ll 1$, this can be written as

$$k_\perp^2 \simeq \frac{1}{\tau\left(\eta_i-\frac{2}{3}\right)}. \quad (37)$$

Having described the two branches of the ITG instability, we now analyze the solution of the ITG dispersion relation, Eq. (33), that includes both of them. In Fig. 3, we show the growth rate, solution of Eq. (33), for $\omega_\kappa = 2k_y$, normalized to $\eta_i R/L_n$, i.e., $\hat{\gamma}k_y = \gamma/(\eta_i R/L_n)$, as suggested by Eq. (35), and maximized over k_y and $k_\parallel$, as a function of R/L_n and η_i, and for τ ranging from 1 to 4. The normalized growth rate, $\hat{\gamma}k_y$, can be expressed, following the results for the sITG, as $\hat{\gamma}k_y \simeq g(\tau)k_y$. We find that $\hat{\gamma}k_y$ decreases with τ, despite the fact that $g(\tau)$ increases with τ, because k_y decreases with τ. In fact, our numerical results confirm that the poloidal wavenumber, k_y, decreases with τ and η_i, according to Eq. (37), being the k_y at the maximum growth rate inversely proportional to $\sqrt{\tau\eta_i}$.

The normalized parallel wavenumber at the peak growth rate, $k_\parallel/(\eta_i R/L_n)$, is found to be a decreasing function of τ; in fact, it can be estimated as $k_\parallel/(\eta_i R/L_n) \simeq f(\tau)k_y$, where both $f(\tau)$, as well as k_y, are decreasing functions of τ. We also observe that both the normalized growth rate, $\gamma/(\eta_i R/L_n)$ and the normalized parallel wavenumber, $k_\parallel/(\eta_i R/L_n)$ are almost independent of η_i and R/L_n for $\eta_i \gtrsim 1$. We remark that, according to Fig. 3, the ITG instability is unstable above a certain η_i threshold, that decreases with R/L_n, and for values $R/L_n \gtrsim 15$ it is given by $\eta_i \simeq 1$.

As an aside, we note that a second instability, which develops at $k_y \gtrsim 1$, for small R/L_n and small η_i, is also present in Eq. (33). This mode, dependent on the Boussinesq's approximation used in deducing the vorticity equation (see Eq. (28)) and driven by magnetic curvature, is typically overpowered by the ITG instability. We exclude this mode from the analysis that follows, as it appears in a parameter regime that is not of relevance for SOL turbulence.

IV. ESTIMATE OF THE EQUILIBRIUM PRESSURE GRADIENT

We now determine an estimate of the equilibrium pressure gradient. We use the same methodology described in Ref. 36, based on the gradient removal theory,[24,25,36,37] which assumes

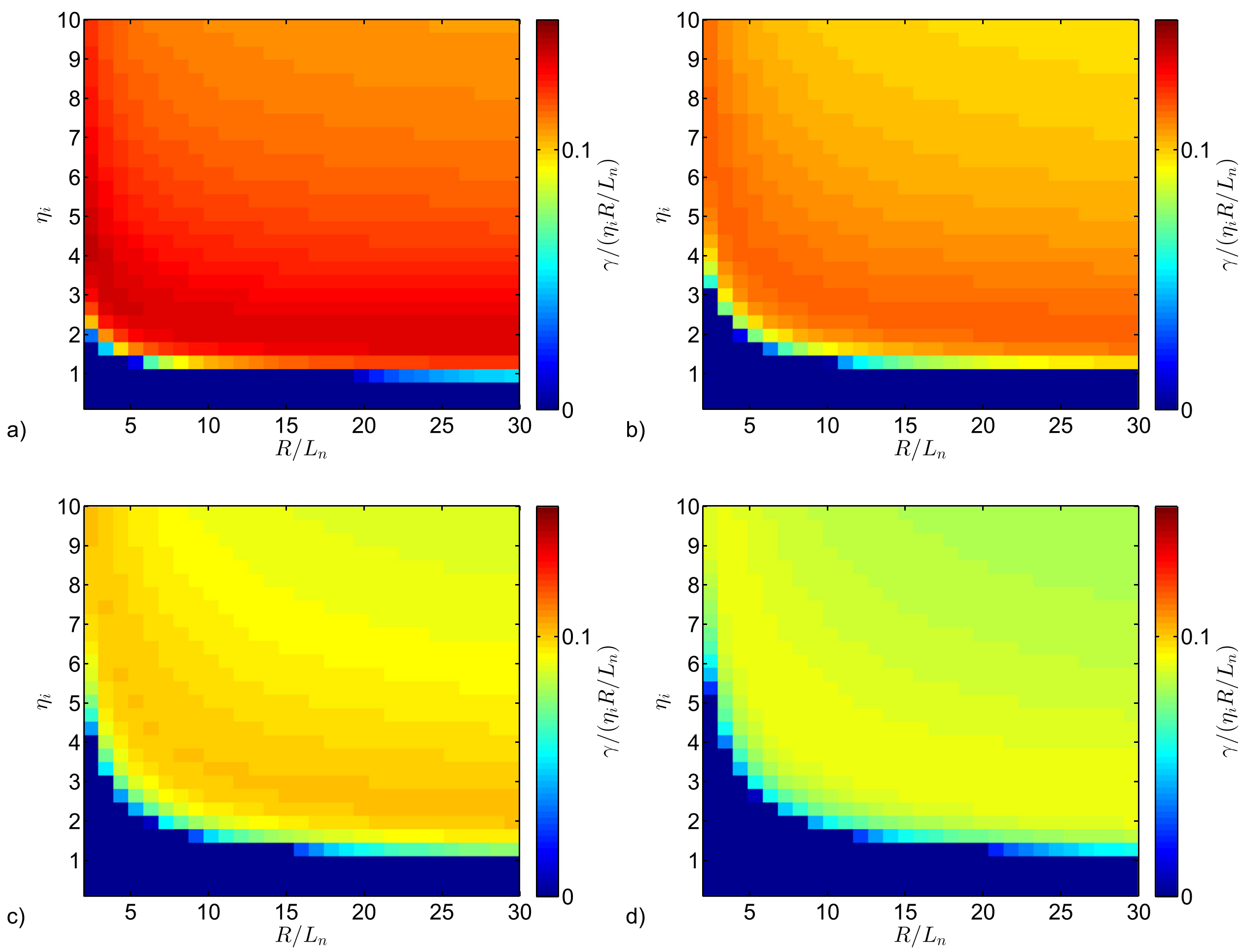

FIG. 3. Normalized growth rate $\hat{\gamma}k_y = \gamma/(\eta_i R/L_n)$ for the ITG mode, solution of Eq. (33) as a function of η_i and R/L_n for $\tau = 1$ (a), $\tau = 2$ (b), $\tau = 3$ (c), and $\tau = 4$ (d).

that turbulence saturation occurs when the background time-averaged pressure radial gradient is comparable to the perturbed pressure radial gradient, $k_x\tilde{p} \sim \bar{p}/L_p$, where k_x gives the typical radial extension of the pressure fluctuations, and tilde and overbar are used to indicate the fluctuations and the background components, respectively. The range of applicability of the gradient removal hypothesis in estimating the turbulent saturation level, versus other mechanisms, e.g., Kelvin-Helmholtz secondary instability, is discussed in Ref. 24.

From a time, toroidal, and poloidal average of the pressure equation, it is possible to write a balance between radial $E \times B$ transport and parallel losses, $\partial_x \bar{\Gamma}_x \sim \bar{p}\,\bar{c_s}/(qR)$. Estimating the radial $E \times B$ flux as $\bar{\Gamma}_x \sim k_y \overline{\tilde{\phi}\tilde{p}}$, the potential fluctuations from the leading term of the pressure equation, obtained by summing the density and the temperature equations,

$$\gamma\tilde{p} \sim ik_y\tilde{\phi}R/L_p, \tag{38}$$

and the pressure fluctuations from the gradient removal hypothesis, we can derive an estimate of L_p

$$L_p^2 = \frac{\gamma q}{k_x^2 c_s\sqrt{1+\tau}}. \tag{39}$$

We note that, in the present paper, the pressure gradient L_p refers to the total pressure $p = p_e + p_i$. Equation (39) constitutes the equation that provides L_p as a function of the SOL operational parameters, and strongly depends on the linear instability driving the turbulent transport, through the values of γ and k_x. In the following, we estimate L_p by assuming that transport is driven by the ITG instability, $L_{p,ITG}$. We then recall the scaling of L_p when the RBM drives turbulence, $L_{p,RBM}$. Using these results, in Sec. V we deduce the SOL turbulent regimes, and we identify the SOL turbulence driving instability.

To calculate $L_{p,ITG}$ according to Eq. (39), we first estimate the ITG typical radial extension of the unstable mode, k_x. Applying the non-local linear method outlined in Ref. 38, we write the dispersion relation of the ITG, taking Eq. (33), in the $k_\parallel \to 0$ limit for simplicity, as

$$\frac{\partial^2\phi}{\partial x^2} - k_y^2[1+G(x)]\phi = 0, \tag{40}$$

where

$$G(x) = \frac{-\gamma - 2ik_y(1+\tau) + ik_yR/L_n - \dfrac{2ik_y\tau\left[2\gamma + i(-2+3\eta_i)k_yR/L_n\right]}{3\gamma + 10ik_y\tau}}{\gamma k_y^2\left\{1 + \dfrac{\tau\left[2\gamma + i(-2+3\eta_i)k_yR/L_n\right]}{3\gamma + 10ik_y\cdot\tau}\right\}}. \tag{41}$$

Then, we Taylor expand $G(x)$ around x_0, the point of steepest gradient

$$G(x) \simeq G_0 + G_0''(x-x_0)^2/2, \tag{42}$$

obtaining a harmonic oscillator equation, $\partial_x^2\phi - k_y^2[1 + G_0 + G_0''(x-x_0)^2/2]\phi = 0$, whose solution can be written as

$$\phi \sim \exp\left[\frac{-a(x-x_0)^2}{2}\right], \tag{43}$$

being

$$a = k_y\sqrt{\frac{|G_0''|}{2}}, \tag{44}$$

and where $G_0'' = \partial_x^2 G(x)$. The estimate of the ITG radial eddy extension is $k_x = \sqrt{a}$. The $L_{p,ITG}$, evaluated according to Eq. (39), is shown in Fig. 4(a), where γ is evaluated from Eq. (33), in the $k_\parallel \to 0$ limit, and G_0'' has been evaluated by deriving Eq. (41).

A simplified scaling law for $L_{p,ITG}$ can be analytically obtained to explain qualitatively the results in Fig. 4(a). The growth rate, γ, solution of Eq. (33), is developed to the lowest order in k_y, and in the limit $R/L_n \gg 1$, that is

$$\gamma = k_y\left(\frac{iR}{2L_n} + \frac{1}{6}\sqrt{-\frac{9R^2}{L_n^2} + \frac{72\eta_i R\tau}{L_n} - 160\tau^2}\right), \tag{45}$$

while the k_x estimate is obtained from Eq. (44), in the limit $R/L_n \gg 1$, and considering only the lowest order terms in k_y, obtaining

$$k_x^2 = \sqrt{\frac{9(1+\eta_i\tau)}{2L_n^2(3+2\tau)^2}}. \tag{46}$$

Comparing Eq. (46) to the radial mode number estimate for BM and DW, $k_x \simeq \sqrt{k_y/L_p}$,[39–41] we note that the radial extension of the ITG is the macroscale $\lambda_x \sim L_p$, while for the BM and DW is the mesoscale $\lambda_x \sim \sqrt{L_p/k_y}$. Substituting Eqs. (45) and (46) into Eq. (39), we obtain a polynomial equation for L_p

$$aL_p^4 + cL_p^2 + dL_p + e = 0, \tag{47}$$

$$\begin{aligned} a &= 18(1+\tau)(1+\eta_i\tau),\\ c &= 160/9k_y^2q^2(3+2\tau)^2(1+\eta_i)^2\tau^2,\\ d &= -8k_y^2q^2R\eta_i\tau(3+2\tau)^2(1+\eta_i),\\ e &= 4k_y^2q^2R^2(3+2\tau)^2. \end{aligned} \tag{48}$$

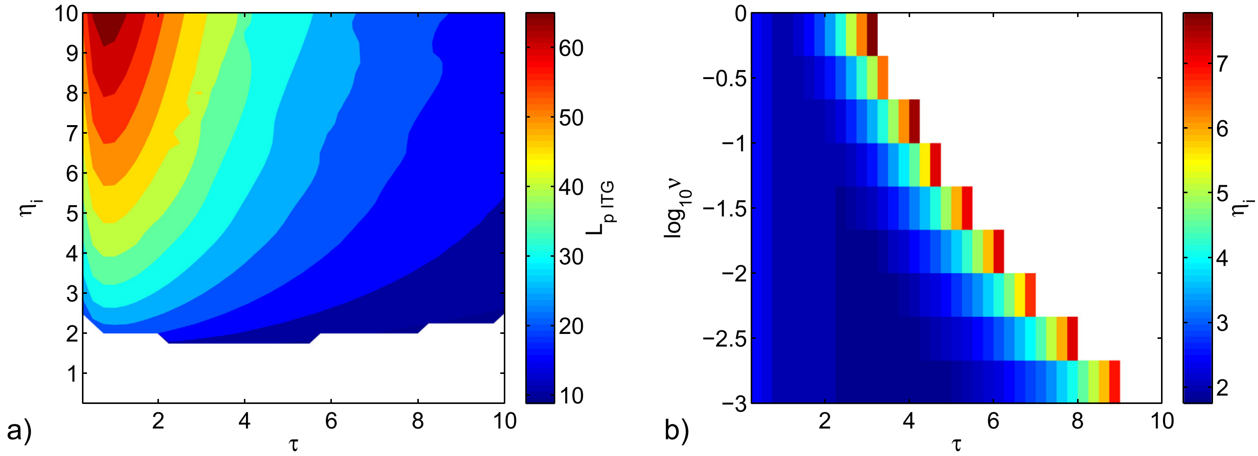

FIG. 4. Estimate of the equilibrium pressure scale length, L_{pITG}, from Eq. (39), in the hypothesis of ITG modes driving turbulence and transport (a). η_i threshold above which the turbulence is driven by the ITG (b).

For large τ, the L_p estimate can be evaluated as a balance between the second and the first order terms, leading to

$$L_{p,ITG} \sim \frac{9R\eta_i}{20\tau(1+\eta_i)}. \tag{49}$$

Equation (49) describes qualitatively the $L_{p,ITG}$ estimates shown in Fig. 4(a): $L_{p,ITG}$ decreases with τ, and increases with η_i, becoming weakly dependent on η_i at large values of η_i.

We recall that a scaling law for $L_{p,RBM}$ has been obtained in Ref. 37. Starting from Eq. (39) and assuming $\gamma \simeq \gamma_B^{max}$, $k_x = \sqrt{k_y/L_p}$, and $k_y \simeq k_y^{min}$ (see Sec. III B), the following scaling law $L_{p,RBM}$ is derived

$$L_{p,RBM} = \frac{R^{3/7}}{\rho_{s0}} 2^{3/7} q^{8/7} (1+\tau)^{1/7} \nu^{2/7}. \tag{50}$$

The RBM gradient length estimate from Eq. (50) has been compared to a large number of non-linear SOL simulations performed with the GBS code, covering a wide range of SOL parameters in the $\tau = 0$ limit, showing good agreement.[37,42] Moreover, Eq. (50) estimates have been compared against experimental results of the Alcator C-MOD, Compass, JET, TCV, and Tore Supra tokamaks, also showing good agreement.[37]

V. SCRAPE-OFF LAYER TURBULENT REGIMES

In the following, we evaluate the SOL turbulent regimes by identifying the linear instability driving the SOL turbulence, demonstrating that the ITG instability is non-linearly overpowered by the RBM instability. The instability driving turbulence in the SOL is expected to be the one leading to the largest L_p, since it allows the system to relax to the state with the lowest turbulent drive. Therefore, we expect that turbulence is driven by the ITG when $L_{p,ITG} > L_{p,RBM}$. In Fig. 4(b), we show the η_i threshold above which $L_{pITG} > L_{pRBM}$ as a function of τ and ν, evaluated according to the results showed for the ITG case in Fig. 4(a), and Eq. (50) for the RBM case. At low τ and ν, turbulence is driven by ITG modes at $\eta_i \gtrsim 2$ and the η_i threshold increases with τ and ν. Finally, in the white area, for high τ and ν, the RBM always drives transport.

This analysis confirms therefore our predictions based on the linear result: the ITG instability is active in the SOL when η_i overcomes a threshold that depends on τ and ν, being in any case $\eta_i \gtrsim 2$ necessary to have development of ITG-driven turbulence.

It turns out that the value of η_i in the SOL can be theoretically estimated by generalizing the method described in Ref. 40. We consider the leading terms in the density, the electron temperature, and the ion temperature equations, neglecting curvature and diffusion terms, since smaller than the radial $\boldsymbol{E} \times \boldsymbol{B}$ turbulent transport and the parallel advection terms. We can therefore write, by time, toroidally, and poloidally averaging the density equation

$$\frac{\partial \bar{\Gamma}_n}{\partial x} \simeq -\frac{1}{2\pi q R} \overline{nV_{\parallel e}}|_{\text{limiter}}, \tag{51}$$

where $\partial_x \bar{\Gamma}$ is the radial $E \times B$ turbulent flux, toroidally and poloidally averaged, while $\overline{nV_{\parallel e}}|_{\text{limiter}}$ is the toroidally and time averaged parallel flux of n evaluated at the two limiter plates. The same notation is used for the T_e and T_i parallel fluxes, i.e., $\overline{T_e V_{\parallel e}}|_{\text{limiter}}$ and $\overline{T_i V_{\parallel e}}|_{\text{limiter}}$. Analogously, for the electron temperature equation it is possible to write

$$\frac{\partial \bar{\Gamma}_{T_e}}{\partial x} \simeq -\frac{2}{3}\frac{1}{2\pi q R} \overline{T_e V_{\parallel e}}|_{\text{limiter}}, \tag{52}$$

and for the ion temperature equation,

$$\frac{\partial \bar{\Gamma}_{T_i}}{\partial x} \simeq -\frac{2}{3}\frac{1}{2\pi q R} \overline{T_i V_{\parallel e}}|_{\text{limiter}}. \tag{53}$$

Similar to the pressure $E \times B$ turbulent flux, we can write $\bar{\Gamma}_n$, as

$$\bar{\Gamma}_n = k_y \overline{\tilde{n}\tilde{\phi}}. \tag{54}$$

The density fluctuations, $\tilde{n}$, are estimated from the leading order term of the continuity equation as $\tilde{n} \sim \tilde{\phi}\bar{n}Rk_y/(\gamma L_n)$, $\tilde{\phi}$ using Eq. (38), and $\tilde{p}$ according to the gradient removal theory, $\tilde{p}/\bar{p} = 1/(k_x L_p)$. Inserting these approximations into Eq. (54), the radial density turbulent flux becomes

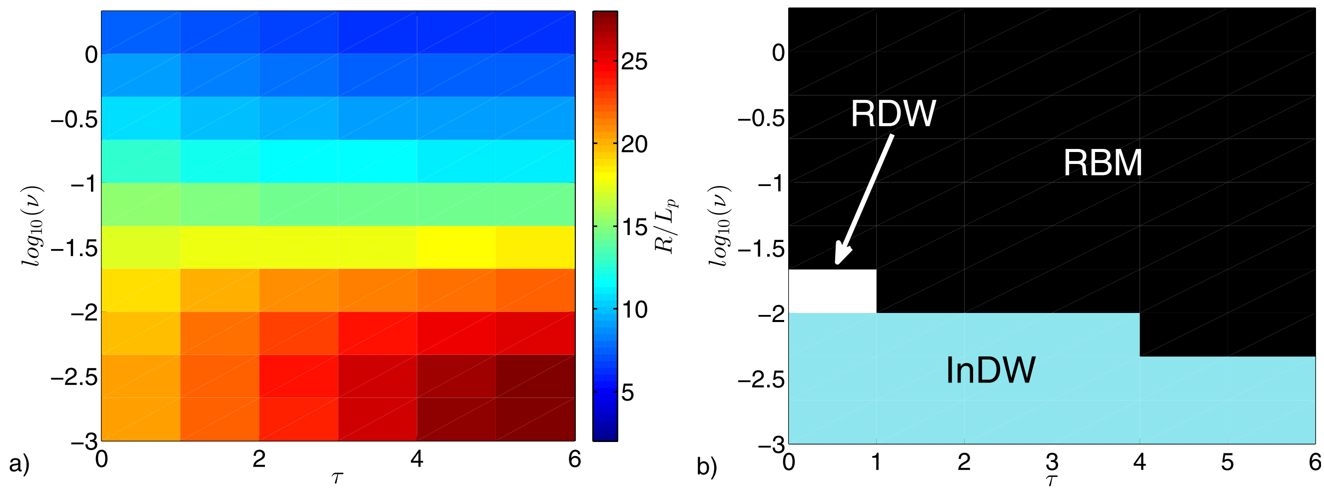

FIG. 5. R/L_p estimate (a) and turbulent regimes (b) at $m_i/m_e = 1836$; different colors identify different regimes: RBM (black), RDW (white), and InDW (light blue).

$$\bar{\Gamma}_n \sim \frac{\gamma \bar{n}}{k_x^2 R L_n}, \tag{55}$$

and analogous expressions can be written for $\bar{\Gamma}_{T_e} \sim \gamma \overline{T_e}/(k_x^2 R L_{T_e})$ and $\bar{\Gamma}_{T_i} \sim \gamma \overline{T_i}/(k_x^2 R L_{T_i})$. We assume that n admits solutions in the form $\bar{n} = n_{max} \exp[(x - x_s)/L_n]$ for $x > x_s$, where x_s is the radial position of the source, and corresponds to the location of the last closed flux surface. Analogous assumptions are made for T_e and T_i. Moreover, we write the linear growth rate as $\gamma = f \overline{T_e}^{1/2}$, where $f = f(R/L_p, \eta_e, \eta_i)$, and depends also on the SOL operational parameters. This representation is valid for all the linear instabilities under investigation. Substituting the expressions for $\bar{n}$, $\overline{T_e}$, $\overline{T_i}$ and for γ into Eq. (55), we obtain

$$\frac{\partial \bar{\Gamma}_n}{\partial x} = \frac{f \bar{n}_{max} \bar{T}_{e,max}^{1/2}}{k_x^2 R L_n} \left(\frac{1}{L_n} + \frac{1}{2L_{T_e}} \right) \exp\left[(x - x_s) \left(\frac{1}{L_n} + \frac{1}{2L_{T_e}} \right) \right], \tag{56}$$

and analogous expressions can be written for $\partial_x \bar{\Gamma}_{T_e}$ and $\partial_x \bar{\Gamma}_{T_i}$. Inserting Eq. (56), and similar ones for $\partial_x \bar{\Gamma}_{T_e}$ and $\partial_x \bar{\Gamma}_{T_i}$ into Eqs. (51)–(53), we obtain

$$\begin{aligned} \frac{f}{k_x^2 L_n} \left(\frac{1}{L_n} + \frac{1}{2L_{T_e}} \right) &= \frac{1}{2\pi q}, \\ \frac{3f}{2k_x^2 L_{T_e}^2} &= \frac{1}{3\pi q}, \\ \frac{f}{k_x^2 L_{T_i}} \left(\frac{1}{L_{T_i}} + \frac{1}{2L_{T_e}} \right) &= \frac{1}{3\pi q}, \end{aligned} \tag{57}$$

where we have approximated $\overline{nV_{\parallel e}}|_{\mathrm{limiter}} \sim n_{max} T_{e,max}^{1/2} \exp\left[(x - x_s) \left(\frac{1}{L_n} + \frac{1}{2L_{T_e}} \right) \right]$. Analogous estimates are used for $\overline{T_e V_{\parallel e}}|_{\mathrm{limiter}}$ and $\overline{T_i V_{\parallel e}}|_{\mathrm{limiter}}$. Combining Eq. (57), we obtain that $\eta_e = \eta_i$ and that η_e is the solution of a second order equation in the form

$$\eta_e^2 - \frac{2}{9}\eta_e - \frac{4}{9} = 0, \tag{58}$$

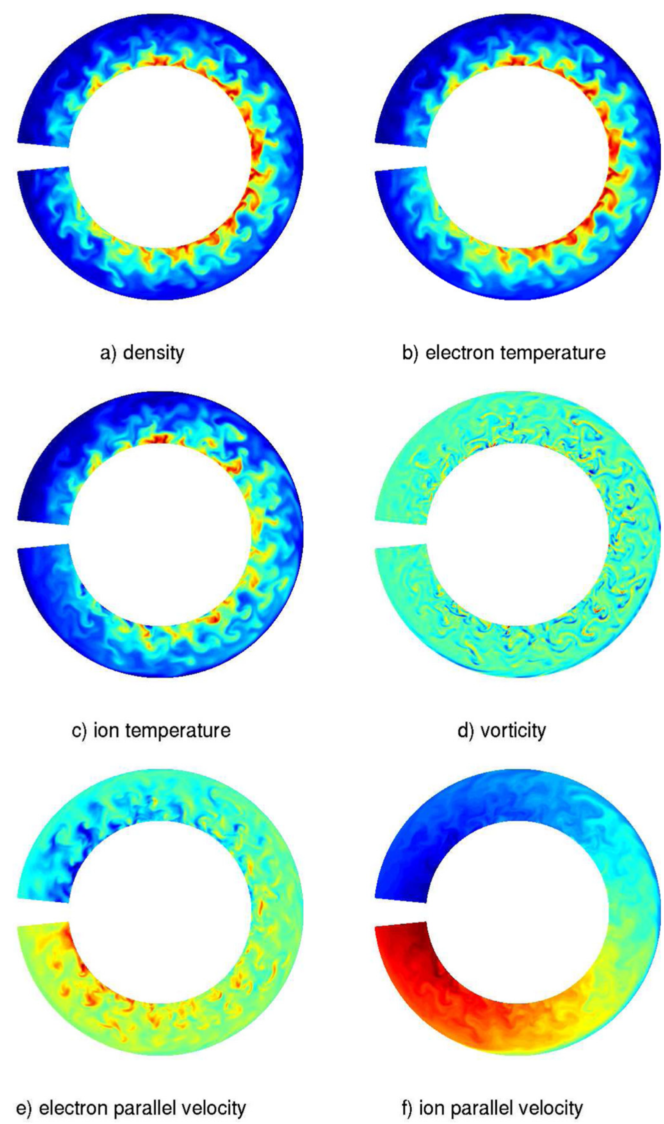

FIG. 6. Snapshots of density (a), electron temperature (b), ion temperature (c), vorticity (d), electron parallel velocity (e), and ion parallel velocity (f), in a poloidal cross section for the non-linear simulation with $\tau = 1$.

that gives $\eta_e = \eta_i = 0.79$. As this value is smaller than the η_i value required for the development of the ITG instability, shown in Fig. 4(b), we conclude that RBM constitutes a stronger turbulence drive than the ITG. As a matter of fact, this also proves that the ITG mode is sub-dominant with respect to the DW in the case the latter dominates over the RBM.

We now identify the SOL turbulent regimes in the presence of hot ions following the same technique described in Ref. 36, concentrating on DW and BM only. We first calculate the equilibrium pressure gradient length resulting from the interplay of turbulent transport and parallel losses using Eq. (39). Since we focus on DW and BM only, we can estimate the radial wavenumber as $k_x \simeq \sqrt{k_y/L_p}$, as discussed in Refs. 39, 40, and 41. Equation (39) results in

$$L_p \sim \frac{q}{c_s\sqrt{1+\tau}}\left(\frac{\gamma}{k_y}\right)_{max}. \tag{59}$$

We consider the theoretically estimated values $\eta_e = 0.79$ and $\eta_i = 0.79$, ν varying between 10^{-3} and 1, τ varying between 0 and 5, $q = 4$, and in Fig. 5(a) we plot the value of L_p evaluated according to Eq. (59). We use the obtained values of R/L_p and k_y to calculate the growth rate of RBM, InBM, RDW, and InDW. The instability driving turbulence is expected to be the one with the largest growth rate. We observe that the RBM drives turbulence for $\nu \gtrsim 5\times10^{-3}$, while for lower values of ν the InDW prevails. The RDW appears at $\nu = 10^{-2}$ and $\tau = 0$.

VI. NON-LINEAR TURBULENCE SIMULATIONS

In order to support the validity of the turbulent regimes identified in Sec. V, we perform a series of non-linear simulations, having set $\nu = 0.1$, $m_e/m_i = 1/200$, $L_y = 800$, $L_x = 100$, and $R = 500$, while τ is varied from 0 to 4. In Fig. 6, we present a snapshot of the different fields evolved during the simulation with $\tau = 1$ in a poloidal cross section: the density, n, the electron temperature, T_e, the ion temperature, T_i, the vorticity, ω, the electron parallel velocity, $V_{\parallel e}$, and the ion parallel velocity, $V_{\parallel i}$.

The plasma injected from the core is transported radially by streamers elongated in the radial direction. This is visible in the density, electron, and ion temperature snapshots (the similarity of these snapshots is not surprising, since the nature of the equations governing these quantities is similar). The analysis of the ion and the electron parallel velocities shows that the particles flow towards the limiter plates, with fluctuations of the electron parallel velocity being larger than the ion ones, due to the higher electron mobility.

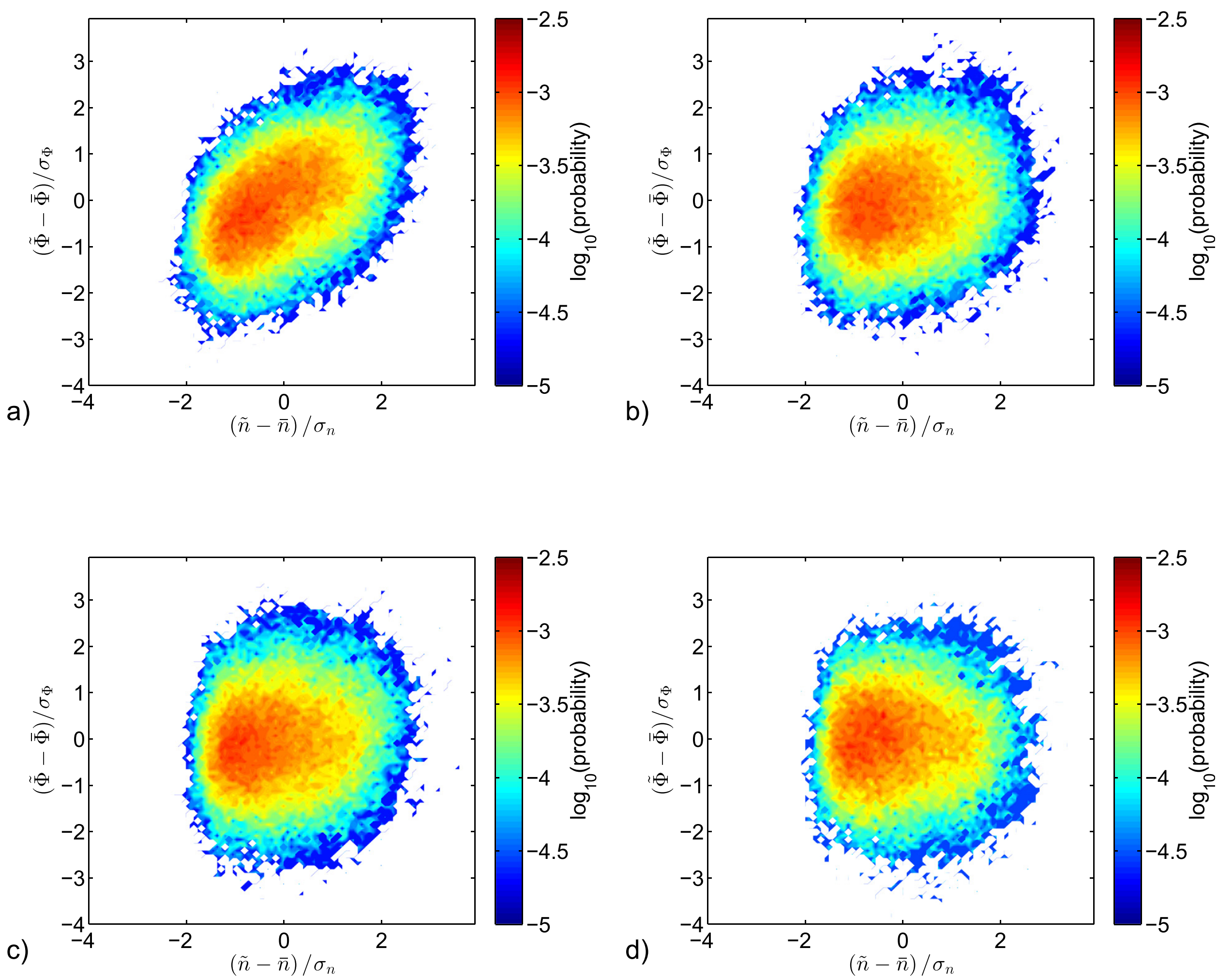

FIG. 7. Joint probability between $\tilde{\phi}$ and $\tilde{n}$ for $\tau = 1$ (a), $\tau = 2$ (b), $\tau = 3$ (c), and $\tau = 4$ (d).

In order to have a first insight into the nature of the turbulent transport, we compute the joint probability between $\tilde{n}$ and $\tilde{\phi}$ in Fig. 7, and their phase shift in Fig. 8, for $\tau = 1, 2, 3$, and 4, according to the methodology explained in Ref. 36. For all the considered values of τ, we observe that there is not a clear correlation between the two fluctuations; moreover, the phase shift between them is close to $\pi/2$. These results are the footprint of a ballooning type of instability (see Ref. 36). This confirms the results of Sec. V, obtained by using the gradient removal theory method presented in Ref. 24.

In Table I, we summarize the most important results coming from our simulations, among which the pressure gradient length, R/L_p, and the mode number in the poloidal direction, k_y. We observe that both R/L_p and k_y values are almost independent of τ. In order to test the validity of our predictions, we compare R/L_p and k_y of the non-linear simulations to the gradient removal estimates from Eq. (59). The maximum difference of R/L_p between our prediction and the simulation results is of the order of 10%. The uncertainty affecting k_y is estimated by considering a 10% variation of the γ/k_y value with respect to its maximum at the predicted R/L_p, and evaluating the k_y range corresponding to this variation. In Table I, we also list the growth rates of each instability separately, in order to identify the instability regime of the non-linear simulations. We observe that the turbulence is RBM driven in all simulations. Finally, in Table I the values of η_e and η_i computed from non-linear simulation results are listed. We note that, η_e decreases from $\eta_e \sim 0.72$ to $\eta_e \sim 0.55$, for τ from $\tau = 0$ to $\tau = 4$, while η_i decreases from 0.59, for $\tau = 1$, to 0.31, for $\tau = 4$. By comparing these values with the theoretical estimates $\eta_e = \eta_i = 0.79$, computed in Sec. V, we observe that, while the theoretical estimate is definitely good for η_e, the simulation values of η_i are in general smaller than the theoretical estimate, particularly at large τ. We have found that this is due to a curvature term, $-10\tau\overline{T_i C(T_i)}/(3R)$, presented in the T_i equation and neglected in Eq. (53). In fact, the parallel outflow terms appearing in Eq. (53) can be estimated as follows:

$$\frac{2}{3}\frac{1}{2\pi qR}\overline{T_i V_{\parallel e}}|_{\text{limiter}} \sim \frac{2}{3}\frac{1}{2\pi qR}\overline{T_i}\sqrt{\overline{T_e}(1+\tau)}, \qquad (60)$$

while for the curvature term we have

$$\frac{10}{3R}\tau\overline{T_i}C(T_i) \sim \frac{10\tau}{3R}\frac{\overline{T_i}^2}{2\pi L_{T_i}}, \qquad (61)$$

where the poloidal gradient of T_i has been neglected with respect to the radial gradient. The ratio of the parallel outflow term with respect to the curvature term is

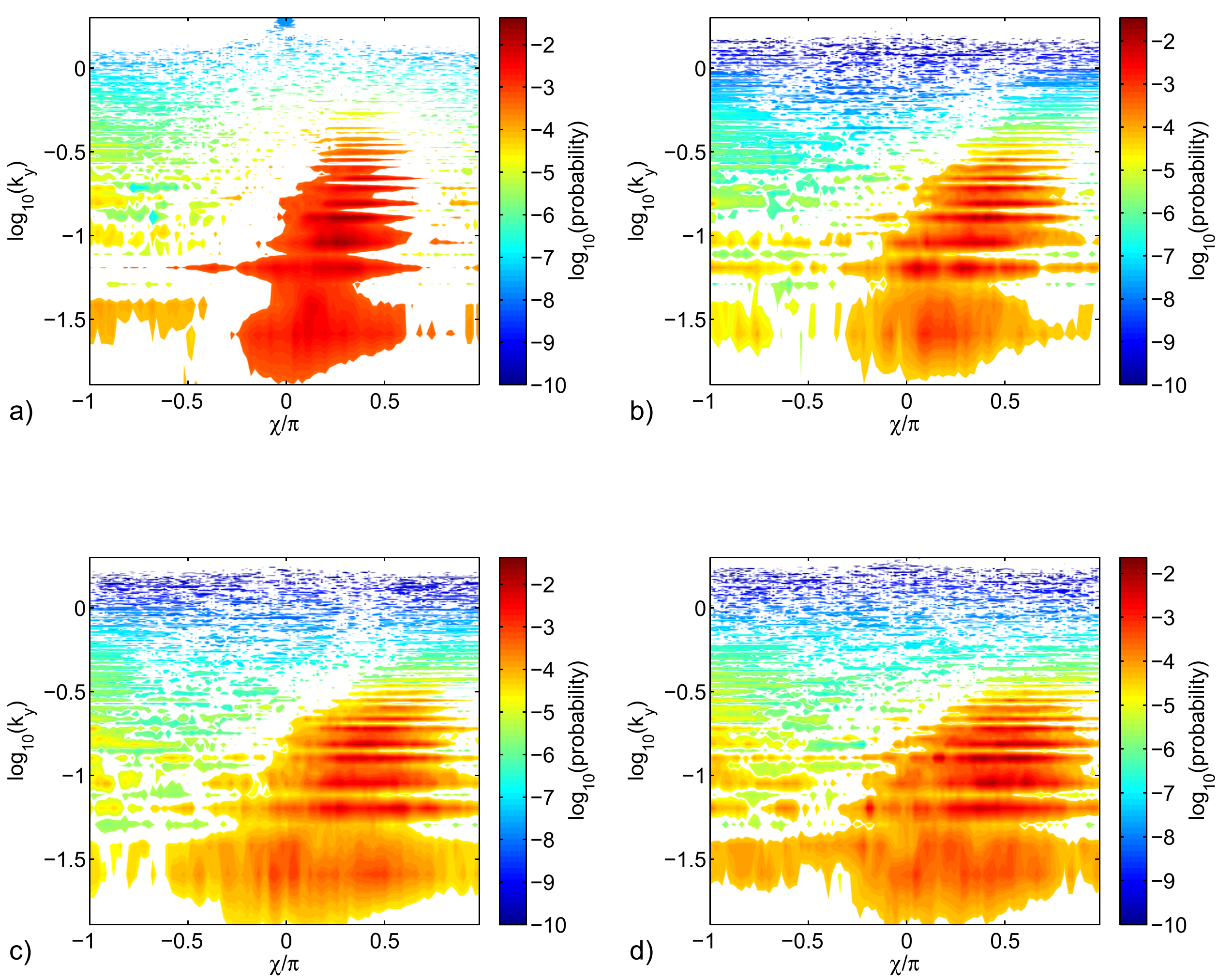

FIG. 8. Phase shift between $\tilde{\phi}$ and $\tilde{n}$ for $\tau = 1$ (a), $\tau = 2$ (b), $\tau = 3$ (c), and $\tau = 4$ (d).

TABLE I. Parameters for the non-linear simulations ($\nu = 0.1$, $m_e/m_i = 1/200$ in all cases). The domain dimensions are $L_y = 800$ and $L_x = 100$. The major radius is $R = 500$. The major radius to the pressure gradient length ratio, R/L_p, is evaluated by fitting n, T_e, and T_i with an exponential function $0 < x - x_s < 70$. The radial window over which k_y is evaluated is $5 < x - x_s < 17$. The two values $k_{y,min}$ and $k_{y,max}$ are computed considering the k_y range corresponding to a 10% variation of the value γ/k_y with respect to its maximum at the R/L_p and k_y predicted.

τ	η_e	η_i	R/L_p simulation	R/L_p estimated	k_y simulation	k_y estimated	$k_{y,min}$ estimated	$k_{y,max}$ estimated	γ_{RBM}	γ_{IBM}	γ_{RDW}	γ_{IDW}	γ_{ITG}
0	0.72	…	12.34	11.94	0.13	0.18	0.13	0.26	2.35	$\simeq$0	0.99	$\simeq$0	…
1	0.64	0.59	12.34	11.30	0.11	0.17	0.11	0.24	2.94	$\simeq$0	0.42	$\simeq$0	0.01
2	0.61	0.49	12.56	10.88	0.09	0.15	0.11	0.22	3.70	$\simeq$0	0.48	$\simeq$0	0.36
3	0.57	0.42	12.56	10.59	0.09	0.15	0.10	0.20	4.07	$\simeq$0	0.44	$\simeq$0	0.45
4	0.55	0.31	12.78	10.34	0.09	0.14	0.10	0.19	4.66	$\simeq$0	0.45	$\simeq$0	0.51

$L_{T_i}\sqrt{1+\tau}/(5q\tau)$. Since, from non-linear simulations results, $L_{T_i} \sim 200$, and typically $q \sim 4$, the curvature term is $\sim$10 times smaller than the parallel outflow term for $\tau \simeq 1$, but the two terms can become comparable at larger τ.

From these observations, it emerges that T_i effects have a relatively minor influence on the turbulent properties and that the turbulent regime driving transport for the considered SOL parameters is the RBM, as predicted in Sec. V.

VII. CONCLUSIONS

In the present paper, we discuss the effects of finite ion temperature on SOL turbulence, by using the drift-reduced Braginskii equations, in the electrostatic limit. This study is motivated by experimental observations that show $T_i \gtrsim T_e$ in the SOL. As finite ion temperature introduces the ITG mode, and modifies the properties of the instabilities that exist in the cold ion limit, like the inertial and resistive branches of the DW and of the BM, one might expect an impact on the non-linear plasma dynamics. To address the role of finite ion temperature, we consider a relatively simple scenario: a tokamak SOL limited on the high field side equatorial midplane, with circular magnetic flux surfaces. The model we use is limited to scenarios in which the perpendicular wavelength of the perturbation is longer than the ion gyroradius, $k_\perp \rho_i < 1$, and other kinetic effects, such as wave-particle resonances and trapped particles, are not important. Moreover, our investigation does not consider magnetic shear effects.

The investigation of finite ion temperature on the linear SOL instabilities shows that both the RDW and the InDW growth rates decrease for increasing η_i, with respect to the maximum attainable value. For the two branches of the BM instability, finite ion temperature increases the maximum growth rate, γ_B^{max}, with respect to the cold ion limit. As in the cold ion limit, the BM instability is damped for $k_y < k_y^{min}$, where k_y^{min} is determined by the parallel dynamics stabilization that becomes more important at large η_i. The ITG mode is unstable at η_i above a threshold that decreases with R/L_n, the threshold being $\eta_i \simeq 1$ for $R/L_n \gtrsim 15$. When unstable, the ITG mode shows a growth rate $\gamma \sim \eta_i \omega_*$ at $k_\parallel \sim \eta_i \omega_*$. The k_y corresponding to the maximum growth rate is inversely proportional to $\sqrt{\tau\eta_i}$.

The η_i observed in the non-linear simulations of Sec. VI and theoretically estimated, also in agreement with experimental observations,[10,11] is smaller than the linear threshold for ITG instability. Therefore, we expect ITG to have a negligible role on SOL turbulence. This is confirmed by the analysis of the SOL turbulent regimes. Indeed, by comparing the L_p estimates for the ITG and for the BM, obtained by means of the gradient removal theory, we show that the ITG is either not active, or it is overcome by the BM, unless $\eta_i \gtrsim 2$, being the threshold an increasing function of τ and ν.

In order to assess the validity of our methodology, we present the results of a set of non-linear GBS simulations with hot ions, for τ ranging from 0 to 4. By means of the joint probability analysis between $\tilde{\phi}$ and $\tilde{n}$, and their phase shift, we conclude that the observed instability has the typical footprint of a BM, being ϕ and n weakly correlated and exhibiting a phase shift close to $\pi/2$. Moreover, the comparison between R/L_p from non-linear simulations and the gradient removal estimate shows good agreement. These findings support the validity of our predictions of the RBM being the turbulent regime driving turbulence.

As a consequence, we conclude that, in the SOL scenario considered here, the ITG instability is expected to play a negligible role in driving and regulating SOL turbulence.

ACKNOWLEDGMENTS

We acknowledge useful discussions with M. Kočan. The simulations presented herein were carried out using the HELIOS supercomputer system at Computational Simulation Centre of International Fusion Energy Research Centre (IFERC-CSC), Aomori, Japan, under the Broader Approach collaboration between Euratom and Japan, implemented by Fusion for Energy and JAEA. This work was carried out within the framework of the EUROfusion Consortium. It was supported in part by the Swiss National Science Foundation and received funding from the European Union's Horizon 2020 research and innovation programme under grant agreement number 633053. The views and opinions expressed herein do not necessarily reflect those of the European Commission.

APPENDIX: BOUNDARY CONDITIONS AT THE MAGNETIC PRESHEATH ENTRANCE OF NON-ISOTHERMAL PLASMAS

The derivation of boundary conditions at the magnetic presheath entrance, including hot ion dynamics, in the limit of isothermal ions and electrons, has been the subject of Sec. II B. We now discuss the isothermal hypothesis, showing that the boundary conditions derived in Sec. II B are reasonable. For this purpose, we follow a derivation of the boundary conditions similar to the one presented in the Appendix of Ref. 33, where we include non-isothermal ion and electron dynamics. For sake of simplicity, we consider the case of no gradients along the x direction. We consider the ion continuity equation, the ion and electron parallel velocity equations, and the electron and ion temperature equations. We use the adimensionalization introduced in Sec. II B. The ion continuity equation, Eq. (6), holds also in the case of non-isothermal ions and electrons. The ion parallel momentum equation, Eq. (9), is modified as follows:

$$nV'_{si}\partial_s V_{\|i} + \sin\alpha(n\partial_s\phi + \tau T_i\partial_s n) + \sin\alpha\tau n\partial_s T_i = S_{\|m_i}, \tag{A1}$$

the last term on the left hand side representing the non-isothermal ion contribution. The electron parallel velocity equation, Eq. (11), is also modified, obtaining

$$\mu\sin\alpha T_e\partial_s n - \mu\sin\alpha n\partial_s\phi + 1.71\mu n\sin\alpha\partial_s T_e = S_{\|m_e}, \tag{A2}$$

the last term on the left hand side representing the non-isothermal electron contribution. The electron temperature equation is derived from the electron temperature equation in Eq. (1), in steady state, neglecting inertia, diffusion, and resistivity effects

$$\begin{aligned} &nV_{\|e}\sin\alpha\partial_s T_e + \frac{2}{3}T_e\big[1.71n\sin\alpha\partial_s V_{\|e} \\ &\quad - 0.71n\sin\alpha\partial_s V_{\|i} + -0.71\big(V_{\|i} - V_{\|e}\big)\sin\alpha\partial_s n\big] \\ &\quad + \frac{2}{3}\sin\alpha\partial_s q_e = S_{T_e}. \end{aligned} \tag{A3}$$

We note that in Eq. (A3) two terms account for the microscopic electron heat flux: the term $-2\cdot 0.71/3T_e(V_{\|i} - V_{\|e})\sin\alpha\partial_s n$, and the term $2/3\sin\alpha\partial_s q_e$. While the first term is calculated according to Braginskii closure, supposing a perturbed Maxwellian distribution for the electrons (see Ref. 43), the second term is associated with the deviation from a Maxwellian distribution function due to the sheath physics. For sake of simplicity, in the present derivation we assume that these two contributions can be summed. To evaluate q_e, we note that when a plasma is in contact with an absorbing wall, a non-neutral sheath develops, where the electrostatic potential drops, causing the repulsion of the electrons. As the electrons having an energy higher than the potential barrier can flow out from the system, without being reflected, the electron population can be described as a truncated Maxwellian. The heat flux in the direction parallel to the magnetic field, associated with the truncated Maxwellian distribution, can be expressed as (see Ref. 44)

$$q_e = \frac{nT_e^{3/2}}{\sqrt{2\pi}I(\eta)}\left(\frac{m_i}{m_e}\right)^{1/2}\left[e^{-\eta}\left(\eta - \frac{1}{2}\right) + \frac{3}{2}\sqrt{\frac{\eta}{\pi}}\frac{e^{-2\eta}}{I(\eta)} + \frac{e^{-3\eta}}{2\pi I^2(\eta)}\right], \tag{A4}$$

where $\eta = \phi/T_e$, and $I(\eta) = [1 + \mathrm{erf}(\sqrt{\eta})]$. The last term on the left hand side of Eq. (A3) can therefore be written as

$$\frac{2}{3}\sin\alpha\partial_s q_e = \frac{2}{3}\sin\alpha\frac{1}{T_e}\partial_s\phi\partial_\eta q_e. \tag{A5}$$

Introducing Eq. (A4) into Eq. (A5), we obtain

$$\frac{2}{3}\sin\alpha\partial_s q_e = \frac{2}{3}\sin\alpha\frac{1}{\sqrt{2\pi}}n\sqrt{T_e}\sqrt{\frac{m_i}{m_e}}A_1\partial_s\phi, \tag{A6}$$

where A_1 is

$$A_1 = \frac{\partial}{\partial\eta}\left(\frac{1}{I(\eta)}\left[e^{-\eta}\left(\eta - \frac{1}{2}\right) + \frac{3}{2}\sqrt{\frac{\eta}{\pi}}\frac{e^{-2\eta}}{I(\eta)} + \frac{e^{-3\eta}}{2\pi I^2(\eta)}\right]\right). \tag{A7}$$

Finally, the ion temperature equation is derived from the ion temperature equation in Eq. (1), where $\boldsymbol{V}_{pol}$ is neglected in $\boldsymbol{V}_{\perp i}$

$$\frac{2}{3}T_i\sin\alpha\partial_s V_{\|i} + V_{\|i}\sin\alpha\partial_s T_i = S_{T_i}. \tag{A8}$$

Equations (6), (A1), (A2), (A3), and (A8) can be written as a linear system of equations, $\boldsymbol{MX} = \boldsymbol{S}$, where $\boldsymbol{X} = (\partial_s n, \partial_s V_{\|i}, \partial_s\phi, \partial_s T_e, \partial_s T_i)$, $\boldsymbol{S}$ is the source vector, and the M matrix is

$$M = \begin{pmatrix} V'_{si} & n\sin\alpha & 0 & 0 & 0 \\ \sin\alpha\tau T_i & nV'_{si} & n\sin\alpha & 0 & \sin\alpha\tau n \\ \mu\sin\alpha T_e & 0 & -\mu n\sin\alpha & 1.71\mu n\sin\alpha & 0 \\ \begin{matrix} 2/3\ 0.71T_e\sin\alpha V_{\|e} + \\ -2/3\ 0.71T_e\sin\alpha V_{\|i} \end{matrix} & -2/3\ 0.71nT_e\sin\alpha & \begin{matrix} 2/3\ 1.71c_\phi nT_e\sin\alpha + \\ +n\sqrt{T_e}A_2\sin\alpha \end{matrix} & \begin{matrix} 2/3\ 1.71c_{T_e}nT_e\sin\alpha + \\ +nV_{\|e}\sin\alpha \end{matrix} & 0 \\ 0 & 2/3\ T_i\sin\alpha & 0 & 0 & V_{\|i}\sin\alpha \end{pmatrix}, \tag{A9}$$

where $A_2 = 2A_1\sqrt{m_i}/(3\sqrt{2\pi m_e})$. In Eq. (A9), we have assumed that $\partial_s V_{\|e} = c_\phi\partial_s\phi + c_{T_e}\partial_s T_e$, where $c_\phi = \partial_\phi V_{\|e}$ and $c_{T_e} = \partial_{T_e}V_{\|e}$ are known functions.[33] Imposing again $\det M = 0$ at the magnetic presheath entrance, we find

$$V_{\|i}^2 = T_e\frac{0.19 + 1.14\hat{c_{T_e}} + \tau\tau_{se}\big[3.25\hat{c_\phi} + 3.1\hat{c_{T_e}} + 5/3 + 2.85A_2\big]}{1.14(1.71\hat{c_\phi} + \hat{c_{T_e}}) + 1 + 1.71A_2}, \tag{A10}$$

where $\tau_{se} = T_i/T_e$ at the magnetic presheath entrance, $\hat{c_\phi} = c_\phi T_e/V_{\parallel e} = -1$, and $\hat{c_{T_e}} = c_{T_e} T_e/V_{\parallel e} = 0.5 + \phi/T_e \simeq 0.5 + \Lambda$. For $\Lambda = 3$, and $m_i/m_e = 1836$, $V_{\parallel i}/c_s$ is a decreasing function of τ, at $\tau = 0$ its value is 1.70, at $\tau = 1$ its value is 1.51, and its limit for $\tau \to \infty$ is 1.29. The previous result shows therefore that the Bohm-Chodura criterion, $V_{\parallel i} = c_s$ at the magnetic presheath entrance does not hold perfectly, even in the $\tau = 0$ limit, when non-isothermal ion and electron dynamics is taken into account. Finally, we can obtain an expression for $\partial_s T_i$

$$\partial_s T_i = \partial_s \phi \frac{\tau_{se}}{F3/2 - 5/2\tau\tau_{se}} \simeq 0.23\, \partial_s \phi, \tag{A11}$$

where $F = V_{\parallel i}^2/T_e$. We remark that the value of $\partial_s T_i$ does not depend on τ. Analogously, we obtain for $\partial_s T_e$

$$\partial_s T_e = \partial_s \phi \frac{1.71 + 3/2\, A_2 - 0.71/(F - \tau\tau_{se})}{1.71(0.5 + \Lambda) + 3/2}. \tag{A12}$$

The function $\partial_s T_e$ increases with τ. At $\tau = 0$, we find $\partial_s T_e/\partial_s \phi \simeq 1 \times 10^{-3}$, at $\tau = 1$ $\partial_s T_e/\partial_s \phi \simeq 0.015$, and in the limit $\tau \to \infty$, it is $\partial_s T_e/\partial_s \phi \simeq 0.04$. According to Eqs. (A11) and (A12), $\partial_s T_i$ and $\partial_s T_e$ can be therefore neglected in comparison with $\partial_s \phi$, confirming the validity of the derivation of the boundary conditions presented in Sec. II B.

[1] M. Kočan, J. P. Gunn, S. Carpentier-Chouchana, A. Herrmann, A. Kirk, M. Komm, H. W. Müller, J.-Y. Pascal, R. A. Pitts, V. Rohde, and P. Tamain, "Measurements of ion energies in the tokamak plasma boundary," in *Proceedings of the 19th International Conference on Plasma-Surface Interactions in Controlled Fusion* [J. Nucl. Mater. **415**(1, Suppl.), S1133 (2011)].

[2] S. Y. Allan, S. Elmore, A. Kirk, M. Kočan, and P. Tamain, "Ion energy measurements on MAST using a midplane RFEA," in *Proceedings of the 20th International Conference on Plasma-Surface Interactions in Controlled Fusion Devices* [J. Nucl. Mater. **438**(Suppl.), S1192 (2013)].

[3] K. Kreuger, Z. H. Huang, M. Jiang, G. S. Xu, W. Zhang, H. Q. Wang, J. Cheng, W. Y. Hong, L. W. H. Yan, and C. Xiao, "Simultaneous ion temperature and flow measurements using a retarding field analyzer in the HL-2A tokamak," Radiat. Effects Defects Solids **168**(10), 776 (2013).

[4] P. Tamain, M. Kočan, J. Gunn, A. Kirk, J.-Y. Pascal, and M. Price, "Ion energy measurements in the scrape-off layer of MAST using a retarding field analyzer," in *Proceedings of the 19th International Conference on Plasma-Surface Interactions in Controlled Fusion* [J. Nucl. Mater. **415**(1, Suppl.), S1139 (2011)].

[5] M. Kočan, S. Y. Allan, S. Carpentier-Chouchana, P. de Marné, S. Elmore, T. Franke, J. P. Gunn, A. Herrmann, A. Kirk, M. Kubič, T. Lunt, H. W. Müller, R. A. Pitts, V. Rohde, and the ASDEX Upgrade Team, "Ion energies and currents of type I and mitigated ELMs in the ASDEX Upgrade far scrape-off layer," Nucl. Fusion **52**(2), 023016 (2012).

[6] M. Kočan, F. P. Gennrich, A. Kendl, H. W. Müller, and the ASDEX Upgrade Team, "Ion temperature fluctuations in the ASDEX Upgrade scrape-off layer," Plasma Phys. Controlled Fusion **54**(8), 085009 (2012).

[7] D. Brunner, B. LaBombard, R. M. Churchill, J. Hughes, B. Lipschultz, R. Ochoukov, T. D. Rognlien, C. Theiler, J. Walk, M. V. Umansky, and D. Whyte, "An assessment of ion temperature measurements in the boundary of the Alcator C-Mod tokamak and implications for ion fluid heat flux limiters," Plasma Phys. Controlled Fusion **55**(9), 095010 (2013).

[8] D. Brunner, B. LaBombard, R. Ochoukov, and D. Whyte, "Scanning ion sensitive probe for plasma profile measurements in the boundary of the Alcator C-Mod tokamak," Rev. Sci. Instrum. **84**(5), 053507 (2013).

[9] I. S. Nedzelskiy, C. Silva, P. Duarte, and H. Fernandes, "Simultaneous measurements of the parallel and perpendicular ion temperature with a pinhole probe in the scrape-off-layer of the tokamak ISTTOK," Rev. Sci. Instrum. **83**(3), 033505 (2012).

[10] M. Kočan and J. P. Gunn, "Comparison of scrape-off layer profiles in outboard-versus inboard-limited plasmas in Tore Supra," Plasma Phys. Controlled Fusion **52**(4), 045010 (2010).

[11] K. Uehara, T. Kawakami, H. Amemiya, K. Höthker, A. Cosler, and W. Bieger, "Measurements of ion temperature and flow velocity using symmetric and asymmetric double probes in the boundary plasma of the JFT-2M tokamak," Nucl. Fusion **38**(11), 1665 (1998).

[12] A. Zeiler, "Tokamak edge turbulence," Max-Planck-Institut für Plasmaphysik, IPP 5/88, 1999.

[13] A. Zeiler, J. F. Drake, and B. Rogers, "Non-linear reduced Braginskii equations with ion thermal dynamics in toroidal plasma," Phys. Plasmas **4**(6), 2134 (1997).

[14] A. Zeiler, D. Biskamp, J. F. Drake, and B. N. Rogers, "Transition from resistive ballooning to η_i driven turbulence in tokamaks," Phys. Plasmas **5**(7), 2654 (1998).

[15] K. Hallatschek and A. Zeiler, "Nonlocal simulation of the transition from ballooning to ion temperature gradient mode turbulence in the tokamak edge," Phys. Plasmas **7**(6), 2554 (2000).

[16] A. Zeiler, D. Biskamp, J. F. Drake, and P. N. Guzdar, "Three-dimensional fluid simulations of tokamak edge turbulence," Phys. Plasmas **3**(8), 2951 (1996).

[17] B. Scott, "The nonlinear drift wave instability and its role in tokamak edge turbulence," New J. Phys. **4**(1), 52 (2002).

[18] B. Scott, "Drift wave versus interchange turbulence in tokamak geometry: Linear versus nonlinear mode structure," Phys. Plasmas **12**(6), 062314 (2005).

[19] N. Bisai, R. Singh, and P. K. Kaw, "Scrape-off layer tokamak plasma turbulence," Phys. Plasmas **19**(5), 052509 (2012).

[20] N. Bisai and P. K. Kaw, "Role of ion temperature on scrape-off layer plasma turbulence," Phys. Plasmas **20**(4), 042509 (2013).

[21] B. Scott, "Computation of electromagnetic turbulence and anomalous transport mechanisms in tokamak plasmas," Plasma Phys. Controlled Fusion **45**(12A), A385 (2003).

[22] P. Ricci, F. D. Halpern, S. Jolliet, J. Loizu, A. Mosetto, A. Fasoli, I. Furno, and C. Theiler, "Simulation of plasma turbulence in scrape-off layer conditions: The GBS code, simulation results and code validation," Plasma Phys. Controlled Fusion **54**(12), 124047 (2012).

[23] W. Dorland and G. W. Hammett, "Gyrofluid turbulence models with kinetic effects," Phys. Fluids B **5**(3), 812 (1993).

[24] P. Ricci and B. N. Rogers, "Plasma turbulence in the scrape-off layer of tokamak devices," Phys. Plasmas **20**(1), 010702 (2013).

[25] F. D. Halpern, S. Jolliet, J. Loizu, A. Mosetto, and P. Ricci, "Ideal ballooning modes in the tokamak scrape-off layer," Phys. Plasmas **20**(5), 052306 (2013).

[26] A. N. Simakov and P. J. Catto, "Drift-ordered fluid equations for field-aligned modes in low-beta collisional plasma with equilibrium pressure pedestals," Phys. Plasmas **10**(12), 4744 (2003).

[27] A. N. Simakov and P. J. Catto, "Erratum: 'Drift-ordered fluid equations for field-aligned modes in low-beta collisional plasma with equilibrium pressure pedestals'," Phys. Plasmas **11**(5), 2326 (2004).

[28] G. Q. Yu, S. I. Krasheninnikov, and P. N. Guzdar, "Two-dimensional modelling of blob dynamics in tokamak edge plasmas," Phys. Plasmas **13**(4), 042508 (2006).

[29] K. Bodi, G. Ciraolo, P. Ghendrih, F. Schwander, E. Serre, and P. Tamain, in *38th EPS Conference on Plasma Physics* (2011), p. P1.121.

[30] D. Russell, D. D'Ippolito, and J. Myra, Bull. Am. Phys. Soc. **57**, BP8.00159 (2012).

[31] J. J. Ramos, "General expression of the gyroviscous force," Phys. Plasmas **12**(11), 112301 (2005).

[32] X. Lapillonne, S. Brunner, T. Dannert, S. Jolliet, A. Marinoni, L. Villard, T. Gorler, F. Jenko, and F. Merz, "Clarifications to the limitations of the s-alpha equilibrium model for gyrokinetic computations of turbulence," Phys. Plasmas **16**(3), 032308 (2009).

[33] J. Loizu, P. Ricci, F. D. Halpern, and S. Jolliet, "Boundary conditions for plasma fluid models at the magnetic presheath entrance," Phys. Plasmas **19**(12), 122307 (2012).

[34] A. Mosetto, F. D. Halpern, S. Jolliet, and P. Ricci, "Low-frequency linear-mode regimes in the tokamak scrape-off layer," Phys. Plasmas **19**(11), 112103 (2012).

[35] P. Ricci and B. N. Rogers, "Turbulence phase space in simple magnetized toroidal plasmas," Phys. Rev. Lett. **104**, 145001 (2010).

[36] A. Mosetto, F. D. Halpern, S. Jolliet, J. Loizu, and P. Ricci, "Turbulent regimes in the tokamak scrape-off layer," Phys. Plasmas **20**(9), 092308 (2013).

[37] F. D. Halpern, P. Ricci, B. Labit, I. Furno, S. Jolliet, J. Loizu, A. Mosetto, G. Arnoux, J. P. Gunn, J. Horacek, M. Kočan, B. LaBombard, C. Silva,

and JET-EFDA Contributors, "Theory-based scaling of the sol width in circular limited tokamak plasmas," Nucl. Fusion **53**(12), 122001 (2013).
[38]P. Ricci and B. N. Rogers, "Transport scaling in interchange-driven toroidal plasmas," Phys. Plasmas **16**(6), 062303 (2009).
[39]B. N. Rogers and W. Dorland, "Noncurvature-driven modes in a transport barrier," Phys. Plasmas **12**(6), 062511 (2005).
[40]P. Ricci, B. N. Rogers, and S. Brunner, "High- and low-confinement modes in simple magnetized toroidal plasmas," Phys. Rev. Lett. **100**, 225002 (2008).
[41]P. Ricci and B. N. Rogers, "Three-dimensional fluid simulations of a simple magnetized toroidal plasma," Phys. Plasmas **16**(9), 092307 (2009).
[42]F. D. Halpern, P. Ricci, S. Jolliet, J. Loizu, and A. Mosetto, "Theory of the scrape-off layer width in inner-wall limited tokamak plasmas," Nucl. Fusion **54**(4), 043003 (2014).
[43]S. I. Braginskii, "Transport processes in a plasma," Rev. Plasma Physics **1**, 205 (1965).
[44]J. Loizu, P. Ricci, and C. Theiler, "Existence of subsonic plasma sheaths," Phys. Rev. E **83**, 016406 (2011).